

High-Performing Perovskite/Ruddlesden-Popper Fuel Electrode for High-Temperature Steam Electrolysis

Yousef Alizad Farzin,* Mohamad Khoshkalam, Siyuan Guo, Wolfgang Menesklou, Philipp Röse, and André Weber

Ruddlesden-Popper (RP) oxides have emerged as a promising alternative to Ni cermet electrodes for high-temperature steam electrolysis due to their superior oxide ion mobility and conductivity. Combining RP with perovskite (P) can provide superior electrocatalytic activity toward hydroxide oxidation and reduction reaction, driving higher efficiency in solid oxide cells (SOC). This work provides a novel approach to enhancing SOC performance by employing A-site Ce-substituted $\text{Sr}_{0.6}\text{Pr}_{0.4-x}\text{Ce}_x\text{MnO}_3$ ($x = 0.1-0.3$) electrodes, investigating their phase evolution, crystal properties, and cation oxidation states under oxidizing and reducing atmospheres. X-ray diffraction analysis of heat-treated powder in a reducing atmosphere revealed forming mixed P and RP structures at 600–800 °C for $x = 0.1$ and 0.2, which provides excellent conductivity and electrocatalytic activity. Consequently, outstanding cell performance is achieved, with low polarization resistances of $0.053 \pm 0.004 \text{ } \Omega \text{ cm}^2$ at 800 °C. The voltage response at different current densities in an electrolyte-supported cell revealed a high power density of 1.084 W cm^{-2} in fuel cell operation and a current density of 1.00 A cm^{-2} at the thermoneutral voltage at 850 °C in steam electrolysis. Moreover, a low overpotential degradation rate of 45 mV kh^{-1} demonstrated the remarkable potential of the SPCM electrode as a promising Ni-free candidate for SOC application.

transportable fuels like hydrogen.^[1] Solid oxide cells (SOCs) have been receiving considerable attention as sustainable energy storage and efficient energy conversion devices, generating electricity in the fuel cell (FC) mode and hydrogen in the electrolysis cell (EC) mode.^[2,3] There are several advantages to using SOECs operating between 650 and 800 °C, including lower electricity costs and improved reaction kinetics with increasing temperature without the need for noble metal catalysts. As a result, the power-to-hydrogen conversion efficiency increases.^[1]

The nickel-ytria-stabilized zirconia (Ni-YSZ) as a ceramic-metal electrode is the most mature fuel electrode widely used in SOCs, providing electronic conduction pathways through metallic Ni and ionic conduction pathways through the ceramic YSZ backbone.^[4] Although Ni-YSZ electrodes exhibit outstanding catalytic and electronic conductivity, they are susceptible to degradation under high current densities due to Ni migration and

1. Introduction

A constant increase in global energy consumption has prompted research into converting renewable energy into storable,

agglomeration, as well as low redox stability at high temperatures. As a result of these degradation factors, electrode resistance rapidly increases during prolonged experiments, adversely impacting performance.^[5,6]

Y. Alizad Farzin, S. Guo, W. Menesklou, P. Röse, A. Weber
Institute for Applied Materials – Electrochemical Technologies (IAM-ET)
Karlsruhe Institute of Technology (KIT)
Adenauerring 20b, 76131 Karlsruhe, Germany
E-mail: yousef.farzin@kit.edu

M. Khoshkalam
Department of Energy Conversion and Storage
Technical University of Denmark (DTU)
Anker Engelunds Vej, Lyngby DK-2800 Kgs, Denmark

The ORCID identification number(s) for the author(s) of this article can be found under <https://doi.org/10.1002/aenm.202404843>

© 2024 The Author(s). Advanced Energy Materials published by Wiley-VCH GmbH. This is an open access article under the terms of the [Creative Commons Attribution-NonCommercial-NoDerivs License](#), which permits use and distribution in any medium, provided the original work is properly cited, the use is non-commercial and no modifications or adaptations are made.

DOI: 10.1002/aenm.202404843

Perovskites (P) with mixed ionic and electronic conductivity (MIEC) are the most promising fuel electrode material explored for the application of solid oxide cells.^[7,8] Perovskite oxides possess the advantage of being able to achieve diverse electrochemical properties by tailoring the chemical composition.^[9,10] For instance, Li et al.^[11] investigated the performance of $\text{Pr}_{0.4}\text{Sr}_{0.5}\text{Co}_x\text{Fe}_{0.9-x}\text{Mo}_{0.1}\text{O}_{3-\delta}$ perovskite oxides and revealed the controlled CoFe alloy exsolution under reducing conditions. This in-situ exsolution process led to an increased oxygen vacancy concentration, effectively enhancing the electrocatalytic activity, particularly $\text{Pr}_{0.4}\text{Sr}_{0.5}\text{Co}_{0.1}\text{Fe}_{0.8}\text{Mo}_{0.1}\text{O}_{3-\delta}$ with the highest current density at 1.3 V of $-456.2 \text{ mA cm}^{-2}$ in SOEC mode at 700 °C. Still, some other material systems show a practical improvement in electrochemical properties by in-situ exsolution under reducing conditions, including $\text{La}_{0.4}\text{Sr}_{0.6}\text{Co}_{0.2}\text{Fe}_{0.7}\text{Mo}_{0.1}\text{O}_{3-\delta}$ ^[12] and $\text{La}_{0.65}\text{Sr}_{0.3}\text{Cr}_{0.85}\text{Ni}_{0.15}\text{O}_{3-\delta}$.^[13] These exsolution metal particles are usually embedded on the electrode surface, creating well-bonded interfaces.^[14] This configuration leads to strong interactions

between the metal particles and the oxide matrices, facilitating the transport of electrons and ions across the metal-oxide interface.^[10]

Furthermore, certain perovskite materials undergo the phase transition to a Ruddlesden-Popper (RP) structure in addition to in-situ nanoparticle exsolution under fuel electrode operating conditions.^[15–19] The RP structure consists of alternating rock-salt layers (AO) and perovskite-like layers (ABO₃) along the crystallographic c-axis direction. The perovskite-to-Ruddlesden Popper (P-to-RP) transformation can benefit electrocatalysis due to the high concentration of mobile oxide ions in the RP structure.

The initial studies on RP structure investigated their electrocatalytic activity on the air side of SOCs as an air electrode. The higher ionic conductivity of the RP oxides, such as Pr₂NiO_{4+δ},^[20] La₂NiO_{4+δ},^[21] and Pr₂Ni_{1-x}Nb_xO_{4+δ},^[22] makes it a most promising candidate for intermediate temperature SOC compared to the state-of-the-art La_{0.6}Sr_{0.4}Fe_{0.8}Co_{0.2}O_{3-δ} (LSCF)^[23] and La_{0.58}Sr_{0.4}CoO_{3-δ} (LSC) electrodes.^[24]

Later, a characteristic feature of RP structures attracted researchers to develop a fuel electrode material that would simultaneously be electrocatalytic active and stable under a reducing atmosphere. The idea of developing fuel electrodes rather than perovskites was mainly inspired by the work on Pr_{0.5}Ba_{0.5}MnO_{3-δ} (PBM) perovskite, which transforms to layered perovskite with heat treatment at 800 °C in pure hydrogen.^[25] The operation of the PBM electrode using humidified hydrogen demonstrated a power density of 1.3 W cm⁻² at 850 °C. However, the high operation temperature and required high concentrations of hydrogen hinder its application in steam electrolysis operation.

The presence of Mn at the B-site is reported to be crucial to achieving P-to-RP phase transformation in La_{0.6}Sr_{0.4}Fe_{0.8}Mn_{0.2}O_{3-δ} under a reducing atmosphere at elevated temperatures (i.e., 800 °C).^[16] The Mn ions can also avoid structure break-up due to forming MnO as an intermediate component. A change in the oxidation state of Mn ions due to varying the oxygen partial pressure in steam electrolysis can further improve surface reaction kinetics for H₂O molecule splitting.^[26] However, this hypothesis requires more detailed analyses of actual cell operations before concluding. Besides, Sr substitution at the Ba site improves structural stability, oxygen transport, and conductivity in similar layered perovskites.^[27,28]

Taking these into consideration, Monica et al. investigated the electrochemical performance of the La_{0.5}Sr_{1.5}MnO_{4±δ} (LSM) Ruddlesden-Popper in the hydrogen oxidation reaction at 600–830 °C for symmetrical solid oxide cell.^[26,29] The developed electrode can be operated under oxidizing and reducing atmospheres, simplifying manufacturing and minimizing thermal expansion coefficient mismatch between the cell components. However, the poor electrocatalytic activity of the developed electrode caused a high polarization resistance of 1.04 Ω cm² at 830 °C while operating in 3%H₂O/H₂ gas.

The insufficient surface reaction kinetics of LSM with an RP structure has led to studies to improve electrocatalytic activity by metallic particle exsolution. For instance, the electrochemical performance of La_{1.2}Sr_{0.8}Mn_{0.4}Fe_{0.6}O₄ (LSMF) electrode was investigated by in-situ preparation under H₂ flow.^[30] Accordingly, the exsolution of Fe nanoparticles on the electrode backbone highly improved electrocatalytic activity by increas-

ing the maximum power density of 0.34 to 0.72 W cm⁻² at 800 °C with operation in H₂ fuel. Despite this, the thermal expansion coefficient of the LSMF electrode increases rapidly above 750 °C due to Fe exsolution and variation of cations oxidation state, which becomes a severe obstacle for a stable cell operation.

In another study, Kim et al.^[31] examined the effect of different Ni concentrations on the electrochemical performance of similar electrode material, in which Gd replaces La with the chemical composition of SrGdNi_xMn_{1-x}O_{4±δ} (SGNM) at different concentrations of x = 0.2, 0.5, and 0.8. According to the XPS results, a decrease in x value increased oxygen vacancies, while H₂-TPR results indicated the in-situ formation of the Ni particles on the RP backbone at higher x values. Electrochemical testing of the SGN_{0.2}M_{0.8}-CGO electrode conducted in 3% humidified H₂ showed a power density of 1.26 W cm⁻² at 850 °C, which is promising for the SOFC application. Nevertheless, the author did not investigate the performance of electrodes at higher steam concentrations as part of the SOEC application. An increase in oxygen partial pressure with steam concentration can significantly influence the electrode performance by varying the oxidation state of the ions and the concentration of oxygen vacancies.

Our previous work investigated the electrochemical performance of (Sr,Pr)MnO_{3.4} oxide over a wide range of steam partial pressure to develop active fuel electrode materials with RP structure.^[32] The high electrocatalytic activity with a low polarization resistance was recorded at 610 °C. Moreover, the perovskite (Sr_{0.5}Pr_{0.5}MnO₃) to Ruddlesden-Popper (SrPrMnO_{4±δ}) phase transformation was observed with heat treatment in humidified 5% H₂/N₂ gas at 800 °C. In principle, forming the RP structure increases electrode conductivity in a reducing atmosphere. However, the impedance spectra showed suppression of electrocatalytic activity with increasing temperature to 710–760 °C, indicating that further chemical composition modification is required to achieve stable electrochemical performance in different steam partial pressures.

This work explores a new approach that combines the RP with P phases to develop a highly efficient fuel electrode for steam electrolysis. By combining perovskite, known for its remarkable electrocatalytic activity, with Ruddlesden-Popper, renowned for superior ionic conductivity, we aimed to substantially enhance cell electrochemical performance by minimizing polarization resistance. A key aspect of this approach involves producing P and RP structures from identical cations, thus minimizing the formation of undesired intermediate phases that could affect electrochemical reactions. This strategy ensures the uniform distribution of these structures throughout the electrode structure, facilitating surface reactions and oxygen ion diffusion. For this purpose, the effect of Ce-doping on crystal properties and electrocatalytic activity for Sr_{0.6}Pr_{0.4-x}Ce_xMnO₃ (SPCM) (x = 0.1, 0.2, and 0.3) will be investigated in great detail. We explore the effect of operating temperature in the reducing atmosphere by incorporating Ce into the A-site of the perovskite structure, thereby enhancing the stability of the perovskite and improving the kinetics of electrochemical surface reactions. Furthermore, we investigate the electrochemical performance of SPCM electrodes and degradation mechanisms under a wide range of steam partial pressure (3–60% H₂O in H₂) and temperatures (650–850 °C).

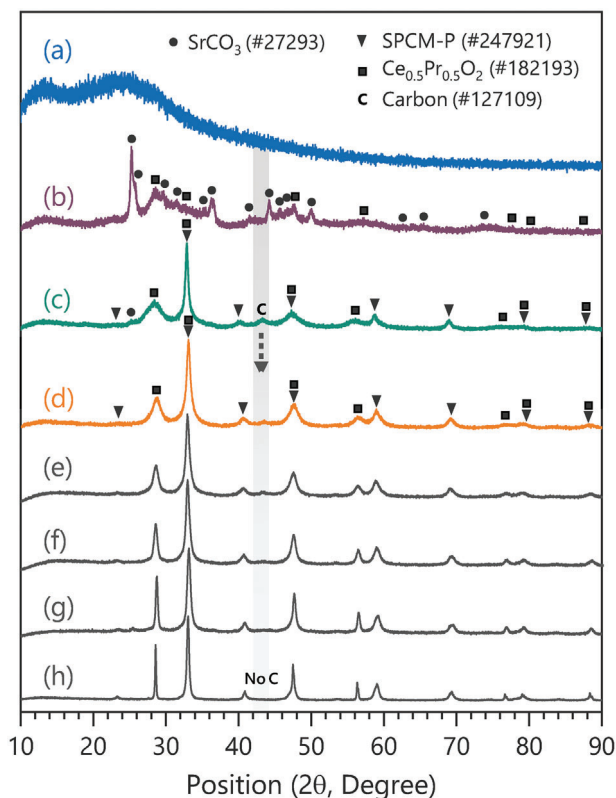


Figure 1. X-ray diffraction patterns of a) produced ash at 300 °C and heat-treated powders at b) 500 °C, c) 600 °C, d) 700 °C, e) 800 °C, f) 900 °C, g) 1000 °C, and h) 1200 °C for 3 h in the air.

2. Results and Discussion

2.1. Phase Formation and Evolution

In order to understand the electrochemical performance of the SPCM electrodes for hydrogen oxidation/reduction, the formation of the perovskite phase in the oxidizing atmosphere will first be discussed, representing the processing conditions to produce the SOCs. A Rietveld refinement analysis will then be applied to in-situ XRD to determine phase evolution under a reducing atmosphere corresponding to the steam electrolysis.

Figure 1 shows the X-ray diffraction patterns obtained for heat-treated powder in the 300 to 1200 °C temperature range in the synthesis of $\text{Sr}_{0.6}\text{Pr}_{0.4-x}\text{Ce}_x\text{MnO}_3$ (SPCM2, $x = 0.2$) perovskite by the sol-gel combustion method. It needs to be highlighted that the phase evolution for all subjected compositions with different Ce concentrations exhibits similar behavior during the combustion and calcination in the temperature range of 25–500 °C. It coincides with removing NO_3^- and C-O bands and forming simple oxides.^[33]

The phase compositions at different temperatures are identified according to the inorganic crystal structure database (ICSD) reference cards. The XRD pattern of the ash powder after combustion with a CA:MI = 1.5 confirms oxidation-reduction reactions produce amorphous powder (Figure 1a).^[34] The carboxyl groups of citric acid and nitrate ions undergo a redox reaction

during combustion, forming simple oxides and eliminating the carboxyl group.^[33,35] However, the excess amount of citrate ions leads to the leftover carbon. The amorphous nature of ash powder makes it impossible to identify the carbon-containing components after combustion. Still, it can be identified with the ICSD #127 109 reference card at higher calcination temperatures.

With increasing the calcination temperature to 500 °C in air, $\text{Ce}_{0.5}\text{Pr}_{0.5}\text{O}_2$ (ICSD #182 193) and SrCO_3 (ICSD #27 293) are observed alongside other phases (Figure 1b). It has also been reported that intermediate phases such as Pr_2O_3 , MnO_2 , and CeO_2 form in the temperature range of 350–500 °C before forming the main perovskite phase.^[36] However, a noisy background complicates phase identification using the standard database reference cards. A sharp peak ($2\theta = 25.26^\circ$) in Figure 1b corresponding to the strontium carbonate suggests that the carbon derived from the excess citric acid interacts with the strontium ions during the combustion.^[37,38]

XRD pattern in Figure 1c indicates that SrCO_3 mainly decomposed when the heat treatment temperature increased to 600 °C. Decomposition of carbonate at similar temperatures range of 540–620 °C was also reported, respectively, for $(\text{Pb}_{0.76}\text{Ca}_{0.24})\text{TiO}_3$ and $(\text{Pb}_{0.50}\text{Ca}_{0.50})\text{TiO}_3$ prepared via sol-gel methods using citric acid as chelating agent.^[39] In another work, residual carbonate components were still observed after heat treatment of Sr-doped LaMnO_3 at 750 °C using sol-gel synthesis.^[40]

In addition, the reaction of intermediate phases at 600 °C leads to the forming of the perovskite $\text{Sr}_{0.65}\text{Pr}_{0.05}\text{Ce}_{0.3}\text{MnO}_3$ (SPCM-P) (ICSD #247 921) with an orthorhombic structure and $\text{Ce}_{0.5}\text{Pr}_{0.5}\text{O}_2$ (CPO) as secondary phase along with residual carbon. With increasing the temperature to 700 °C, the remaining SrCO_3 phase decomposes completely, and the residual carbon content further decreases (Figure 1d). With the exception of the trace amount of residual carbon, quantitative analysis of the XRD results revealed that 26.5 wt.% CPO and 73.5 wt.% SPCM-P are formed at 800 °C (Figure 1e).

The X-ray diffraction pattern at 800 °C shows the CPO secondary phase in all subjected SPCM powders with different Ce concentrations (Figure 1s, Supporting Information). Increasing the Ce concentration intensifies the corresponding peak for the CPO phase. Therefore, using the peak area ratio method, the CPO weight percent in the SPCM1 and SPCM3 powders is calculated at 19.9 wt.% and 33.0 wt.%, respectively. Similarly, the investigation of phase evolution for the $\text{Pr}_{1-x}\text{Ce}_x\text{MnO}_{3\pm\delta}$ ($x = 0, 0.2, 0.4, 0.6, 0.8, 1$) indicated successful replacement of Pr by Ce at the low doping amount ($x \leq 0.4$), whereas Ce-based structure formed when Ce concentration increases above $x = 0.6$.^[36] It should be highlighted that forming the CPO phase can accelerate electrochemical reactions on the electrode surface as a catalyst toward hydrogen oxidation/reduction reaction.

As the calcination temperature increases to 1200 °C (Figure 1e-h), the chemical components of identified phases are not affected, except for peak sharpening of the SPCM and CPO phases. Besides, the corresponding peak intensity of the carbon effectively decreases up to 1000 °C, and it completely disappears at 1200 °C, which is the sintering temperature assigned to the SPCM fuel electrode in this work.

The peaks sharpen with increasing heat treatment temperature, indicating the increased atomic diffusion that leads to

growing crystallinity and particle size. The crystallite size was calculated using the Scherrer equation:

$$D = \frac{K\lambda}{\beta \cos \theta} \quad (1)$$

where D represents the average crystallite size assuming spherical particles, K is the shape factor ($K = 0.9$ [41]), λ is the Cu-K α radiation wavelength ($\lambda = 1.54 \text{ \AA}$ [42]), β is the full width at half maximum (FWHM) of the diffracted peak, and θ is the diffraction angle. It is calculated that the average crystallite sizes of SPCM perovskite and CPO at 800 °C are 11.5 nm and 8.2 nm, respectively. At 1200 °C, these sizes increase to 22.4 nm for SPCM and 47.2 nm for CPO, representing a high crystal growth rate in CPO compared to the SPCM structure.

Incorporating the Ce and Pr from the CPO phase into the SPCM perovskite/Ruddlesden popper lattices depends on their ionic radius difference with Sr in the A sites. The Sr cations occupy the A-site of the perovskite and Ruddlesden-Popper structure with coordination numbers 12 and 9, respectively. According to the literature, the ionic radius of Sr in the perovskite is $\text{Sr}^{2+} (\text{XII}) = 1.44 \text{ \AA}$, and in the Ruddlesden-Popper is $\text{Sr}^{2+} (\text{IX}) = 1.31 \text{ \AA}$. [43] As a result of the oxygen partial pressure, Ce and Pr ions exist in multivalent states within the P and RP structures, with different ionic radius values. [32,44] The ionic radius of Ce in the perovskite is $\text{Ce}^{4+} (\text{XII}) = 1.14 \text{ \AA}$, while the Ruddlesden-Popper possesses $\text{Ce}^{3+} (\text{XII}) = 1.34 \text{ \AA}$ and $\text{Ce}^{3+} (\text{IX}) = 1.196 \text{ \AA}$, depending on its coordination number. [45] Accordingly, the occupation of A-sites by Ce ions in the SPCM structure is most likely possible within the RP structure with negligible crystal lattice distortions.

The ionic radius of $\text{Pr}^{3+} (\text{IX}) = 1.179 \text{ \AA}$ in the RP structure is also closer to the $\text{Sr}^{2+} (\text{IX})$, whereas a huge difference is at the oxidation state of 4+ with an ionic radius of $\text{Pr}^{4+} (\text{VI}) = 0.85 \text{ \AA}$ and $\text{Pr}^{4+} (\text{VIII}) = 0.96 \text{ \AA}$. [45] It suggests that heat treatment in a reducing atmosphere or operating the SPCM electrode in SOC conditions reduces the amount of CPO due to forming the SPCM-RP phase. By introducing an appropriate concentration of Ce doping, the electrodes can achieve optimal electrochemical performance by forming mixed electronic and ionic SPCM-RP surrounded by catalyst particles of CPO and highly electrocatalytic active SPCM-P perovskite. [32]

To investigate the crystalline structure and phase evolution under SOC operation conditions for subjected compositions (SPCM1, SPCM2, and SPCM3), the powders obtained after calcination at 800 °C were further heat-treated in 5% H_2/Ar (with $p\text{O}_2 = 1.86 \times 10^{-22} \text{ atm}$) at a temperature range of 600–800 °C. The XRD results of reduced powder at 600 °C showed a similar diffraction pattern with no phase transformation for SPCM1 and SPCM2 powder (Figure 2s, Supporting Information), whereas the SPCM3 decomposed to CPO, MnO (#18 006), SPCM-P, and SPCM-RP (#237 941) phases. The quantitative analysis of the phases revealed a formation of 26.4 wt.% CPO and 19.2 wt.% MnO in the reduced SPCM3 powder, representing its phase instability for SOC application. We have therefore excluded SPCM3 from further phase analysis and electrochemical study. At the above temperatures, i.e., 700 and 800 °C, the P-to-RP phase transformation is observed for SPCM1 and SPCM2, and the CPO phase reached its minimum value due to inward Ce

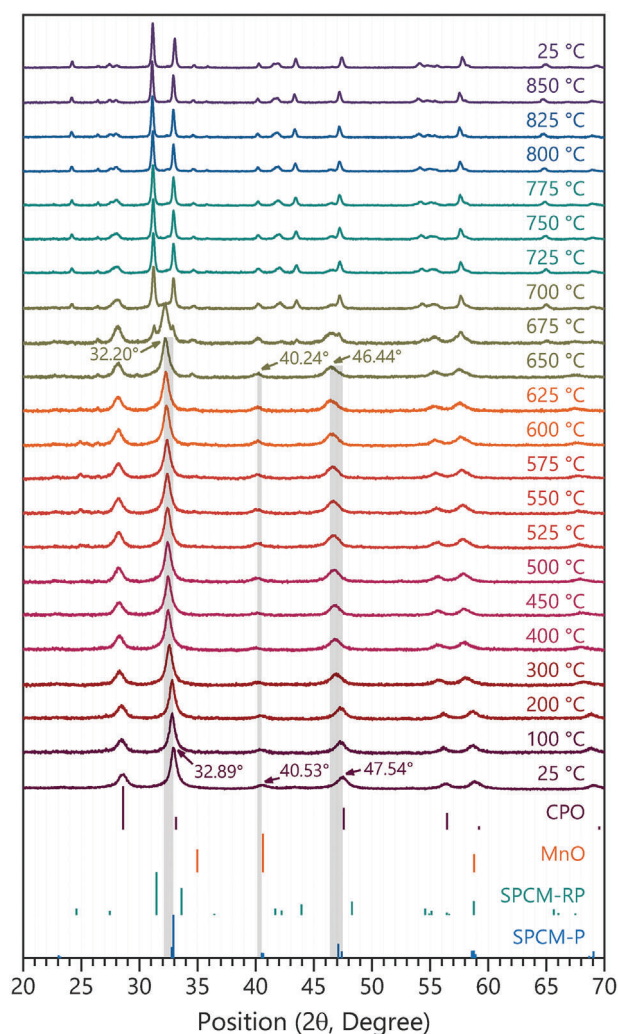


Figure 2. In-situ X-ray diffraction patterns of $\text{Sr}_{0.6}\text{Pr}_{0.2}\text{Ce}_{0.2}\text{MnO}_3$ (SPCM2) powder exposed to 5% H_2/Ar (with $p\text{O}_2 = 1.86 \times 10^{-22} \text{ atm}$) at 800 °C from room temperature up to 850 °C.

and Pr diffusion to the SPCM-RP structure (Figures 3s and 4s, Supporting Information).

The $\text{Sr}_{0.6}\text{Pr}_{0.2}\text{Ce}_{0.2}\text{MnO}_3$ (SPCM2) powder was subjected to further analysis using in-situ XRD, and the results were analyzed by Rietveld refinement to operand study structure evolution and transformation under a similar SOC operation condition. Figure 2 shows the in-situ XRD pattern recorded from room temperature up to 850 °C for SPCM2 powder exposed to a 5% H_2/Ar atmosphere. As shown by the pattern, increasing the temperature up to 450 °C leads the main perovskite peaks at 32.89°, 40.53°, and 47.54° to shift downward, representing expanding the lattice plane distance and crystal parameters in the perovskite structure. At higher temperatures, a further shift has been detected for the diffraction peaks originally located at $2\theta = 32.89^\circ$ and 47.54° , respectively, to $2\theta = 32.20^\circ$ and 46.44° , but the middle peak stays almost at the same diffraction angle ($2\theta = 40.24^\circ$) from 450 °C to 650 °C.

According to the Rietveld refinement (Figure 3a), the crystal parameters for SPCM-P with Orthorhombic structure

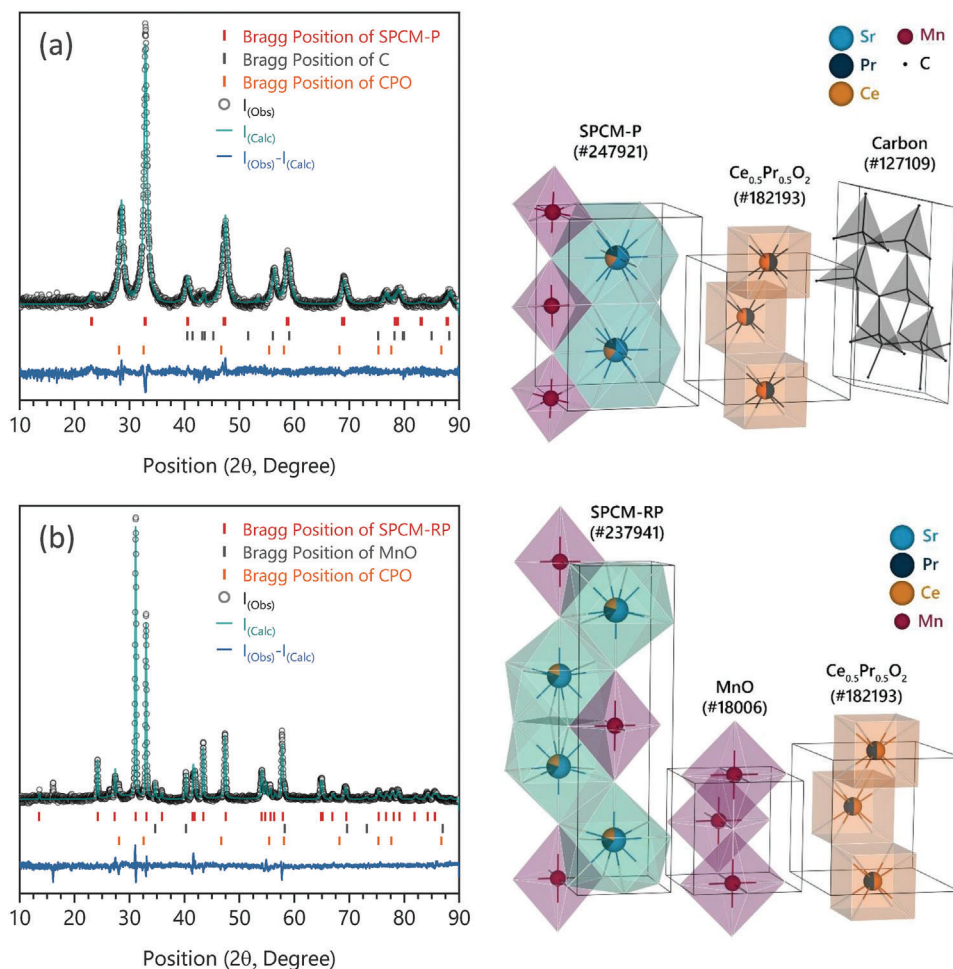


Figure 3. Rietveld refinement profile and crystal structure of formed phases in in-situ XRD of $\text{Sr}_{0.6}\text{Pr}_{0.2}\text{Ce}_{0.2}\text{MnO}_3$ (SPCM2) powder at a) room temperature and b) 850 °C in 5% H_2/Ar (with $p_{\text{O}_2} = 1.86 \times 10^{-22}$ atm at 800 °C). I_{Obs} and I_{Calc} show the X-ray diffraction patterns obtained from the experiment and the calculated profile by Rietveld refinement, respectively.

(Imma (74) space group) are calculated at $a = 5.494$ Å, $b = 7.569$ Å, and $c = 5.585$ Å at room temperature. The details of refined parameters, i.e., the space group, lattice parameters, and site occupancy, are summarized in Table 1s (Supporting Information). From room temperature to 400 °C, the lattice parameters increase continuously to $a = 5.595$ Å, $b = 7.665$ Å, and $c = 5.664$ Å. In contrast to the b and c parameters, the “ a ” parameter shrinks at higher temperatures and reaches its minimum value of 5.475 Å at 650 °C. These variations in crystal parameters versus in-situ XRD at different temperatures are summarized in Table 1 and plotted in Figure 5s (Sup-

porting Information). Instead, the diffraction pattern showed weak peaks corresponding to the MnO and SPCM-RP phases at 650 °C.

As the in-situ analysis temperature increases to 675 °C, the main perovskite peak ($2\theta = 32.20^\circ$) splits into two peaks at 31.24° and 32.91° , corresponding to the partial P-to-RP transformation. Meanwhile, a sharp decrease in the peak intensity of CPO at 700 °C represents the diffusion of the Ce and Pr ions into the A-site of the SPCM-RP structure under the reducing atmosphere (5% H_2/Ar), which is due to dwindling their ionic radius difference to the Sr^{2+} ions in the RP structure.

Table 1. The calculated lattice parameters (a , b , and c (Å)) for the SPCM-P powder (ICSD #247 921) with orthorhombic structure (Imma (74) space group) from in-situ X-ray diffraction pattern at different temperatures (T , °C).

Temperature [°C]	25	100	200	300	400	450	500	525	550	575	600	625	650
Lattice parameters													
a [Å]	5.494	5.518	5.516	5.546	5.595	5.575	5.557	5.536	5.530	5.529	5.507	5.507	5.475
b [Å]	7.569	7.581	7.595	7.642	7.665	7.690	7.701	7.714	7.730	7.731	7.771	7.772	7.818
c [Å]	5.585	5.597	5.604	5.637	5.664	5.669	5.675	5.677	5.686	5.685	5.704	5.703	5.724

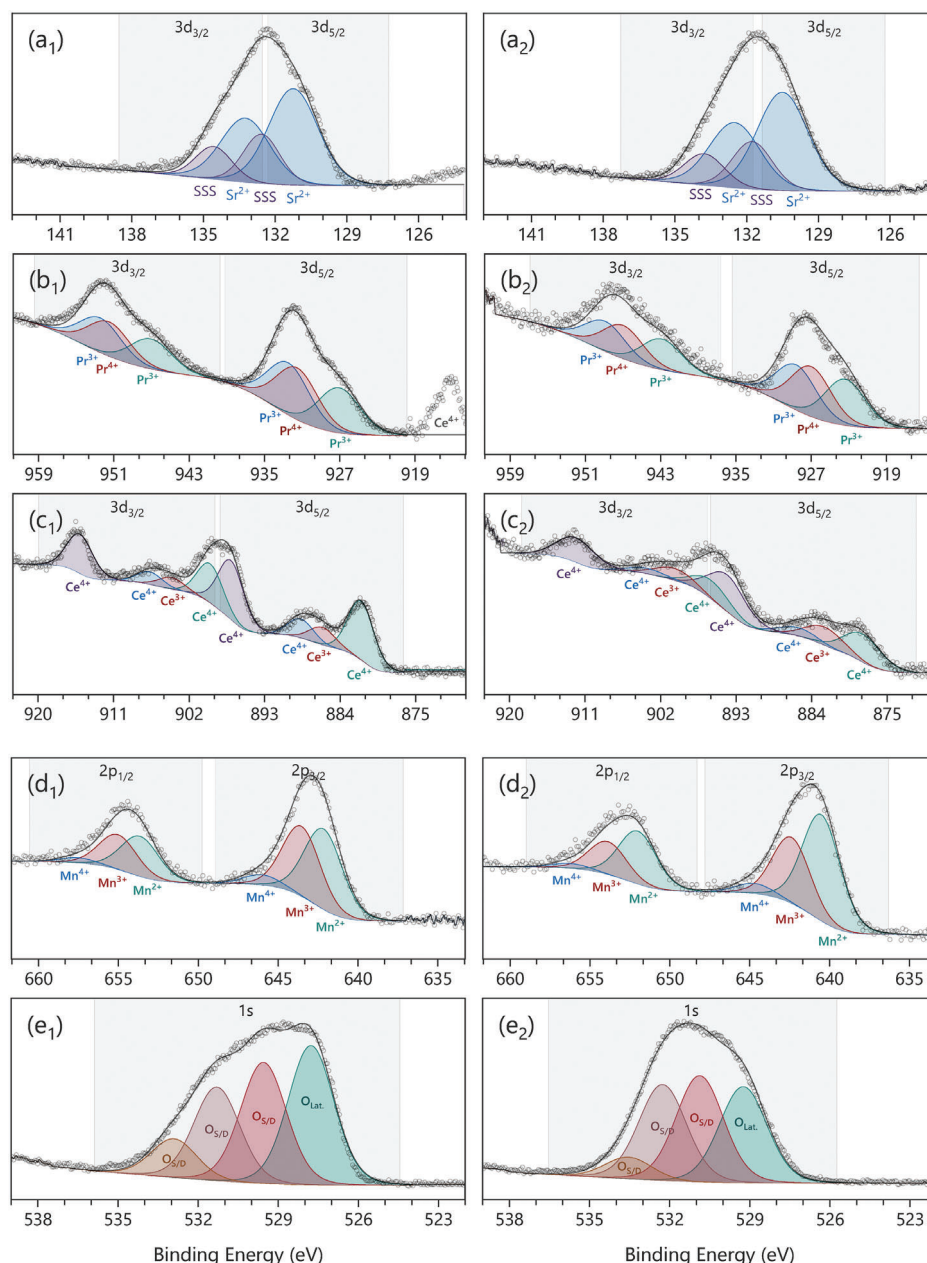
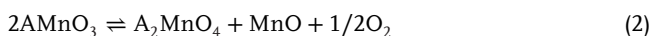


Figure 4. The core-level spectra of a) Sr 3d, b) Pr 3d, c) Ce 3d, d) Mn 2p, e) O 1s for SPCM2 powder. The spectra with numbers 1 and 2 correspond to powder heat-treated at 800 °C in the air with a perovskite structure and in 5% H₂/Ar ($p_{\text{O}_2} = 1.86 \times 10^{-22}$ atm) with a Ruddlesden-Popper structure, respectively. Note: The LA(1.53243) is used as a line shape; the Shirley background is considered for Pr 3d, Ce 3d, and Mn 2p spectra, and the Tougaard background is considered for Sr 3d and O 1s spectra.

According to Equation 2, the P-to-RP phase transformation is reported to coincide with the outward diffusion of B-site cations.^[32,46] In the case of SPCM powder, the diffusion of Mn ions from the B-sites leads to the formation of MnO above 650 °C.



For the reduced powder at 850 °C, the Rietveld refinement resulted in the amount of CPO and MnO phases being 9.3 wt.%

and 6.5 wt.% (Figure 3b). In other words, the formation of RP structure leads to a decrease in the concentration of CPO with inward diffusion of Ce and Pr ions; at the same time, outward diffusion of Mn ions forms MnO under a reducing atmosphere. The crystal parameters for SPCM-RP with Tetragonal structure (I4/mmm (139) space group) are calculated at $a = 3.836$ Å and $c = 13.020$ Å at 850 °C.

Following the XRD measurement at 850 °C, the powder was cooled to room temperature under a 5% H₂/Ar atmosphere, and the XRD pattern was recorded at 25 °C. The obtained results

Table 2. The binding energies, FWHM, percentage contributions, and average oxidation state (AOS) of core electrons for Sr 3d, Pr 3d, Ce 3d, Mn 2p, and O 1s for SPCM2 powder heat-treated at 800 °C in the air with a perovskite structure and in 5% H₂/Ar (pO₂ = 1.86 × 10⁻²² atm) with a Ruddlesden-Popper structure. Note: The LA(1.53243) is used as a line shape; the Shirley background is considered for Pr 3d, Ce 3d, and Mn 2p spectra, and the Tougaard background is considered for Sr 3d and O 1s spectra.

Atmosphere	Spin state	Ions	Binding energy [eV]	FWHM [eV]	Concentration [%]	AOS
Air	3d _{5/2}	Sr ²⁺	131.3	2.4	43.33	2.00 ± 0.03
		SSS	132.8	1.8	16.67	
	3d _{3/2}	Sr ²⁺	133.1	2.4	28.88	11.11
		SSS	134.6	1.8	11.11	
	3d _{5/2}	Pr ³⁺	927.1	5.3	18.17	3.35 ± 0.07
		Pr ⁴⁺	931.5	5.3	20.85	
		Pr ³⁺	932.4	5.3	20.97	
	3d _{3/2}	Pr ³⁺	947.1	5.3	12.11	13.90
		Pr ⁴⁺	951.5	5.3	13.90	
		Pr ³⁺	952.4	5.3	13.98	
	3d _{5/2}	Ce ⁴⁺	881.5	3.6	22.82	3.89 ± 0.08
		Ce ³⁺	886.1	3.6	6.88	
		Ce ⁴⁺	888.7	3.6	7.44	
		Ce ⁴⁺	897.0	3.6	22.86	
	3d _{3/2}	Ce ⁴⁺	899.5	3.6	15.22	4.96
		Ce ⁴⁺	904.1	3.6	4.58	
		Ce ³⁺	906.7	3.6	4.96	
		Ce ⁴⁺	915.0	3.6	15.24	
		Ce ⁴⁺	915.0	3.6	15.24	
	3p _{3/2}	Mn ²⁺	642.2	2.8	33.34	2.47 ± 0.04
Mn ³⁺		643.5	2.8	28.96		
Mn ⁴⁺		646.0	2.8	4.36		
3p _{1/2}	Mn ²⁺	653.8	2.8	16.67	2.18	
	Mn ³⁺	655.1	2.8	14.48		
	Mn ⁴⁺	657.6	2.8	2.18		
1s	O ²⁺ (Lat.)	527.8	2.0	35.43	2.00 ± 0.05	
	O ²⁺ (S/D.)	529.6	2.0	30.79		
	O ²⁺ (S/D.)	531.3	2.0	23.86		
	O ²⁺ (S/D.)	532.9	2.0	9.93		
5% H ₂ /Ar	3d _{5/2}	Sr ²⁺	130.5	2.5	43.28	2.00 ± 0.03
		SSS	132.0	2.0	16.72	
	3d _{3/2}	Sr ²⁺	132.3	2.5	28.85	11.15
		SSS	133.8	2.0	11.15	
	3d _{5/2}	Pr ³⁺	923.4	5.1	19.60	3.35 ± 0.07
		Pr ⁴⁺	927.0	5.1	21.19	
		Pr ³⁺	928.6	5.1	19.21	
	3d _{3/2}	Pr ³⁺	942.9	5.1	13.07	14.13
		Pr ⁴⁺	947.0	5.1	14.13	
		Pr ³⁺	948.9	5.1	12.80	
	3d _{5/2}	Ce ⁴⁺	877.9	5.3	18.33	3.80 ± 0.08
		Ce ³⁺	882.4	5.3	12.02	
		Ce ⁴⁺	885.7	5.3	5.66	
		Ce ⁴⁺	894.1	5.3	24.00	
	3d _{3/2}	Ce ⁴⁺	895.9	5.3	12.22	8.01
		Ce ⁴⁺	900.4	5.3	8.01	
Ce ³⁺		903.7	5.3	3.77		
Ce ⁴⁺		912.1	5.3	16.00		

(Continued)

Table 2. (Continued)

Atmosphere	Spin state	Ions	Binding energy [eV]	FWHM [eV]	Concentration [%]	AOS
	3p _{3/2}	Mn ²⁺	640.5	2.8	38.78	2.57 ± 0.04
		Mn ³⁺	642.4	2.8	24.13	
		Mn ⁴⁺	644.7	2.8	3.76	
	3p _{1/2}	Mn ²⁺	652.1	2.8	19.39	
		Mn ³⁺	654.0	2.8	12.06	
		Mn ⁴⁺	656.3	2.8	1.88	
	1s	O ²⁺ (Lat.)	529.2	2.1	29.99	2.00 ± 0.05
		O ²⁺ (S/D.)	530.9	2.1	33.15	
		O ²⁺ (S/D.)	532.3	2.1	29.99	
		O ²⁺ (S/D.)	533.5	2.1	6.87	

showed no difference in phase composition after cooling down, while the diffraction peaks at $2\theta = 31.09^\circ$ and 32.91° shifted to higher angles of $2\theta = 31.16^\circ$ and 33.06° due to lattice shrinkage (Figure 6s, Supporting Information).

2.2. XPS Analysis

Hydrogen oxidation and reduction are extremely sensitive to the configuration of surface atoms since the electrochemical reactions occur on the electrode surface. Therefore, the XPS measurements were used to determine the oxidation state of the cations in SPCM2 powder. Figure 4 shows the deconvolution of XPS spectra of Sr 3d, Pr 3d, Ce 3d, Mn 2p, and O 1s after heat treatment at 800 °C in the air and in 5% H₂/Ar ($p_{O_2} = 1.86 \times 10^{-22}$ atm) atmospheres. Accordingly, forming perovskite and Ruddlesden-Popper structures in oxidizing and reducing atmospheres helps better understand the electrochemical performance under the SOC operation condition.

The XPS spectra were fitted by Lorentzian line shape, LA(1.53243), using Voigt functions within the Shirley or Tougaard background, and the fitting parameters and quantitative results are summarized in Table 2. The Shirley background assumes that the background intensity is proportional to the total intensity of the XPS signal at the peak's high binding energy, which is ideal for core-level spectra of Pr 3d, Ce 3d, and Mn 2p with low signal-to-noise ratios and moderate inelastic scattering. The Tougaard background accounts for complex inelastic scattering effects, resulting in asymmetrical tails in peaks such as Sr 3d and O 1s spectra.

In order to perform accurate analysis, constrained peaks with equal full width at half maximum (FWHM) were set for each pair of components, and a constant area ratio according to the number of electrons in the p and d orbitals was used to fit the spectra.^[47] Moreover, a fixed doublet separation was applied to fit the cation spectra based on literature data.

The B-site cations generally determine the electrocatalytic activity of perovskites.^[48] Although the cations in the A sites are not involved in the catalytic reaction, based on the XRD results, the varying heat treatment condition highly influences the oxidation state of A-site cations and can also regulate the B-site Mnⁿ⁺ charge. Accordingly, the influence of the heat treatment atmosphere on the oxidation state of the cations on the A-sites will be

discussed, followed by the investigation of the Mn 2p_{3/2} and Mn 2p_{1/2} levels in the P and RP structures.

The core-shell level spectra of the Sr 3d for the P and RP structures are illustrated in Figure 4a. Sr 3d spectra were deconvoluted into surface (Sr surface species, SSS) and lattice components to provide insight into the number of surface species and their evolution under different heat treatment atmospheres. The identified SSS peaks at high binding energies include surface oxides, hydroxides, carbonates, and sulfates.^[49] The area ratio between fitted peaks for the 3d_{3/2} and 3d_{5/2} levels was restricted to 2/3, and a doublet separation of 1.8 eV was used to fit Sr 3d spectra. The FWHM of 2.4 and 2.5 eV is also used for the lattice species in the P and RP structures, respectively.

According to Figure 4a1, the lattice component peaks are located at 131.3 eV and 133.1 eV for 3d_{3/2} and 3d_{5/2} levels, which are correlated with the positions of Sr²⁺ at the perovskite crystal structure.^[50] Formation of the RP structure with heat treating in a reducing atmosphere leads to a shift to lower binding energies of 130.5 eV and 132.3 eV. Comparing the corresponding area for heat-treated powder in the air and reducing atmosphere shows a similar amount of surface species ($27.78\% \pm 0.09\%$) on the P and RP particles. While the XPS analysis was carried out immediately following heat treatment cycles, the interaction of prepared powders with the atmosphere during sample preparation for XPS analysis can also influence the concentration of surface species, which contributed to the similarity of SSS peaks found in this study. The accurate investigation of surface chemistry requires more advanced techniques, including SIMS and LEIS spectroscopy, which is out of the scope of this work.

The scanned Pr 3d spectra display three fitted peaks at 3d_{5/2} and 3d_{3/2} levels corresponding to the Pr³⁺ and Pr⁴⁺ species (Figure 4b). The binding energy at 927.1 and 932.4 eV could be assigned to Pr³⁺ 3d_{5/2}, whereas the peak at 931.5 eV was ascribed to Pr⁴⁺ 3d_{5/2}. Although a significant shift (-4.5 ± 0.4 eV) toward lower binding energy was recorded after forming the RP structure, a neglectable variation in the Pr⁴⁺/Pr³⁺ ratio has been calculated. As a result, the valence state of Pr in SPCM2 powder is not influenced by the heat treatment atmosphere, as both P and RP surfaces have similar average oxidation states (AOS) of $+3.35 \pm 0.02$.

The Ce 3d spectrum (Figure 4c) shows more complicated peaks due to interfered 3d_{5/2} and 3d_{3/2} levels. Six peaks correspond to the three pairs of spin-orbital doublets of Ce⁴⁺, and two

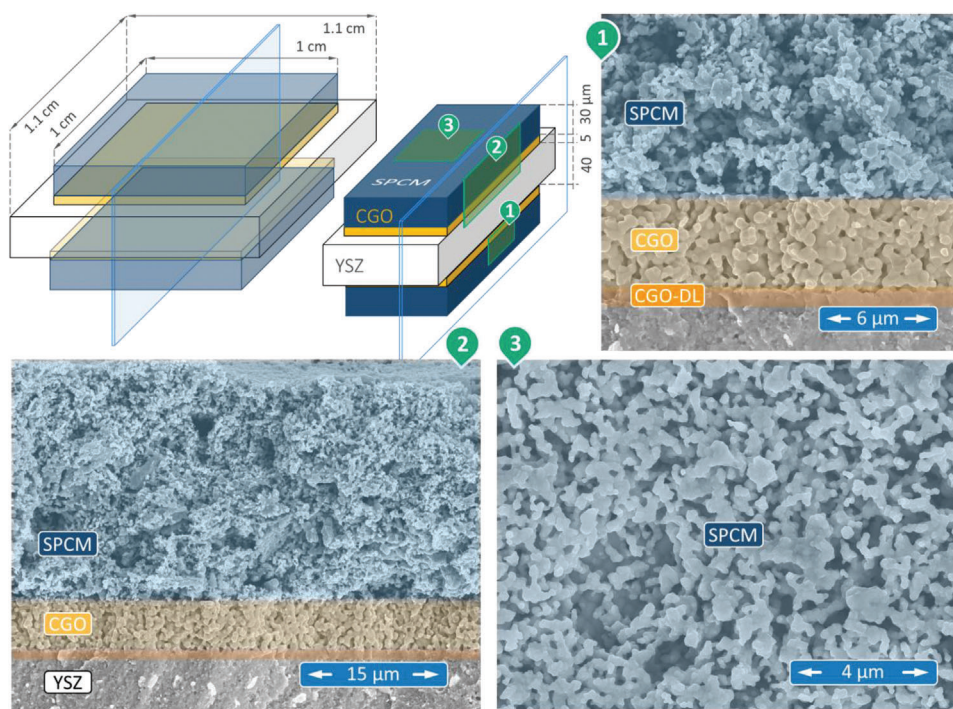


Figure 5. The SPCM2 symmetric-cell schematic with the components' thickness in micrometers and SEM images of the corresponding locations specified in the scheme. The cell was sintered for 3 h at 1200 °C in the air.

peaks reflect the pairs of doublets of Ce^{3+} ,^[51,52] with spin-orbital energy of 18 eV between the pair peaks in the $3d_{5/2}$ and $3d_{3/2}$ orbitals.

The quantitative analysis shows a high concentration of Ce^{4+} (88.54%) after heat treatment in the air, resulting in a significant $\text{Ce}^{4+}/\text{Ce}^{3+} = 7.72$ ratio with an AOS of +3.89 in the perovskite structure. Meanwhile, a high impact of reducing atmosphere to form Ce^{3+} is observed in SPCM2 powder, leading to a decrease in the $\text{Ce}^{4+}/\text{Ce}^{3+}$ ratio to 3.99 and an AOS of +3.80 in the RP structure. As discussed earlier in the phase evolution study, reducing Ce^{4+} ions can decrease the ionic radius mismatch with Sr^{2+} ions in the A sites and lead to inward diffusion of the CPO phase into the RP crystal structure. Since a significant decrease in the CPO phase is identified by Rietveld refinement after reduction, it can be concluded that the large shift (-3.3 ± 0.3 eV) in the Ce 3d orbitals mainly corresponds to binding energies of Ce^{+n} ions in the RP structure.

The Mn 2p spectra (Figure 4d) show three peaks corresponding to the Mn^{2+} , Mn^{3+} , and Mn^{4+} ions in the spin-orbital splitting of the Mn $2p_{3/2}$ and Mn $2p_{1/2}$ levels.^[2,32] The area ratio between fitted peaks for the $2p_{1/2}$ and $2p_{3/2}$ levels was restricted to 0.5, the doublet separation between the peaks at these sub-levels was fixed at 11.6 eV, and an equal FWHM of 2.8 eV was applied for fitting. The quantitative analysis in 2 shows an increase in the concentration of Mn^{2+} species after reduction. Accordingly, the AOS of Mn^{+n} in the P structure decreases from +2.57 to +2.47 in the RP structure. As mentioned earlier, the oxidation state of the ions in the B-sites can be controlled by the heat treatment conditions and the charge compensation caused by variations in the oxidation state of the A-site ions.^[32,48] Accordingly, reducing the A-site ions, specifically form-

ing a high concentration of Ce^{3+} , can highly affect the AOS of the Mn^{+n} ions and the final electrocatalytic activity of the SPCM electrode.

According to the literature, the O 1s spectra could be interpreted as two regions corresponding to the lattice oxygen at lower binding energies and surface components at higher binding energies.^[53,54] As a result, the peak area at high binding energy could reflect the number of oxygen defects at the particles' surface, including oxygen vacancies, adsorbed hydroxide groups, and interstitial oxygen. This work calls these peaks at high binding energies surface species/oxygen defects ($\text{O}_{\text{S/D}}$). The O 1s spectra for heat-treated powder in the reducing atmosphere exhibit intensified peaks at high binding energies and dwindled peak areas corresponding to the lattice oxygen. Accordingly, the ratio of $\text{O}_{\text{S/D}}/\text{O}_{\text{Lat}}$ increases from 1.82 in the P structure to 2.33 in the RP structure. The significant enhancement in the $\text{O}_{\text{S/D}}/\text{O}_{\text{Lat}}$ ratio can be attributed to the characteristic feature of the RP structure, containing high concentrations and mobility of interstitial oxygen.^[55] The high mobility of oxide ions in the RP structure can enhance cell performance by maximizing fuel electrode conductivity under SOC operation conditions.

2.3. Microstructural Investigation

Figure 5 illustrates the microscopy images of the SPCM2 fuel electrode in a symmetric cell configuration, supported by a 3YSZ electrolyte with a thickness of 40 μm . Compared to a conventional electrolyte-supported cell (ESC) containing an electrolyte with a thickness of 80–200 μm , a thinner layer utilized in this study

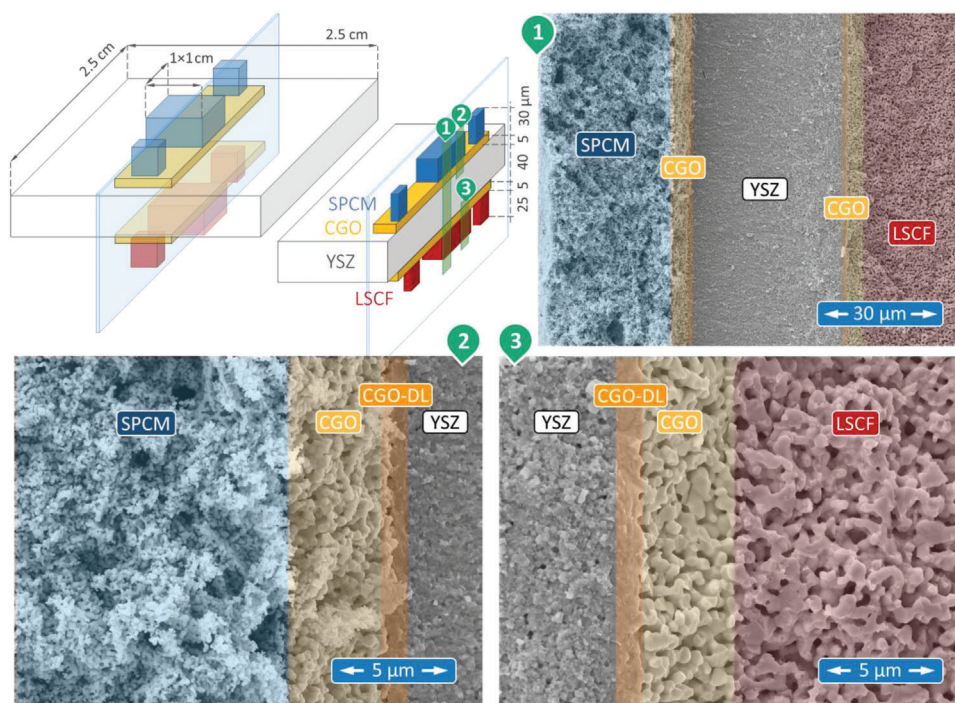


Figure 6. The SPCM2-LSCF full-cell schematic with the components' thickness in micrometers and SEM images of the corresponding locations specified in the scheme. The SPCM fuel electrode was sintered at 1200 °C first, and then the LSCF air electrode was sintered at 1080 °C; both sintering processes were done for 3 h in the air.

can improve the electrochemical performance of solid oxide cell under the operating condition by providing lower electrolyte resistance due to a shorter path for oxide ion diffusion. Moreover, lowered series resistance improves the quality of the impedance spectra and enables a reduced error when analyzing the polarization phenomena in the cell.

A 5 μm CGO barrier layer is applied to both sides of the 3YSZ electrolyte to prevent the interaction of Sr from the electrode with Zr-based electrolytes. The CGO layer is engineered to form a dense interface (CGO-DL) at the CGO/YSZ interface, effectively suppressing SrZrO₃ formation during sintering and electrochemical testing. The CGO-DL is marked with orange in the barrier layer illustration.

After sintering the barrier layer, the screen printing technique applied the SPCM fuel electrode on both sides of the 3YSZ electrolyte. The symmetric cell sintered at 1200 °C exhibits crack-free microstructure with a 30 ± 2 μm thickness. The sintering process results in a well-bonded electrode/electrolyte interface that is crucial to oxide ion conductivity and mechanical stability of the cell. Despite the high sintering temperature, the electrode retains submicron particles with an average size of 310 ± 90 nm, as measured by ImageJ software. This fine particle size enhances the active surface area for hydrogen oxidation/reduction reactions.

Furthermore, the electrode shows good porosity with an average 0.71 ± 0.5 μm pore size covering 41.8% of the electrode structure. These open pores facilitate gas diffusion and minimize gas conversion resistance under the cell operation conditions. Therefore, combining uniformly distributed small particles and open porosity minimizes polarization resistance and enhances the overall electrochemical performance.

After sintering the fuel electrode at 1200 °C, the LSCF air electrode was screen-printed on the other side of the 3YSZ electrolyte to create a full solid oxide cell. **Figure 6** shows the microscopy images of the SPCM2 and LSCF electrodes after the second sintering cycle at 1080 °C in air. The microstructure of the LSCF air electrode shows well-integrated particles to the CGO barrier layer, which makes it difficult to distinguish the LSCF/CGO interface. Similar particle sizes of LSCF electrodes to the CGO barrier layer indicate its high tendency to agglomerate at lower temperatures compared to the SPCM and CGO layers. However, the high catalytic activity of LSCF perovskite toward the oxygen reduction reaction and its mixed ionic and electronic conductivity made it a state-of-the-art electrode for SOC applications, and a small contribution of the air electrode to the final polarization resistance is expected.^[56–58]

It must be highlighted that the Au layer was also applied to the top of the SPCM fuel electrode before conducting the electrochemical testing, and it sintered during the heating up of the cell in the air for testing. The contact layer provides an equipotential surface with the fuel electrode to ensure an excellent electronic connection to the external circuit, including the Ni mesh and Pt wires in the test setup. The Au layer is known as an inert layer while operating the cell for hydrogen oxidation/reduction. Moreover, due to the limited interfacial boundary of the contact layer with the SPCM electrode, which is placed far from the electrode/electrolyte interface, the Au contact layer does not influence the electrochemical reaction kinetics and final cell performance.

On the air side of the cell, there is no need for a contact layer since the LSCF electrode exhibits high electronic conductivity in

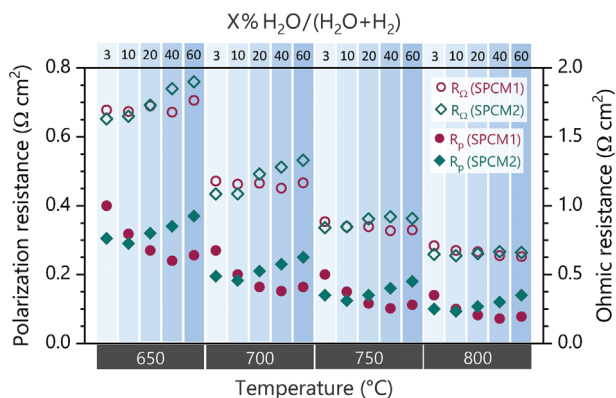


Figure 7. Overview of ohmic resistance (R_{Ω}) and polarization resistance (R_p) extracted from the impedance spectra measured at different temperatures and steam partial pressures for the symmetric cells containing SPCM1 or SPCM2 fuel electrodes. Note: The polarization resistance is provided for two fuel electrodes in a symmetric cell configuration and needs to be divided by two for each electrode.

the oxidizing atmosphere, and Au mesh gets well adhered to the air electrode structure at elevated temperatures (i.e., 650–800 °C). Therefore, the LSCF electrode was connected directly to the Au mesh as a current collector.

2.4. Electrochemical Performance

Impedance spectroscopy was employed to study the electrochemical performance of SPCM fuel electrodes across a temperature range of 650–800 °C and a broad p_{H_2O} range, i.e., 3–60% $H_2O/(H_2O+H_2)$. **Figure 7** displays an overview of the obtained ohmic resistance (R_{Ω}) and polarization resistance (R_p) extracted from Nyquist plots for SPCM1 and SPCM2 fuel electrodes. In which the R_p is provided for two fuel electrodes in a symmetric cell configuration, and thick 3YSZ electrolyte (40 μm) has the main contribution to the R_{Ω} . The variation of R_p with fuel gas composition reveals improving electrochemical performance with steam concentration for the SPCM1 electrode. At the same time, the electrochemical performance degrades for the SPCM2 electrode at higher steam partial pressures. Degradation of R_p for SPCM1 at more reducing atmospheres is mainly due to P-to-RP transformation, which increases the RP/P ratio in the electrode structure. The RP structure features high oxide ion conductivity owing to its mobile interstitial oxygen.^[17,59] However, the electrochemical performance of the RP electrodes is mainly limited due to the poor electrocatalytic activity under reducing conditions for the fuel electrode, requiring a certain amount of P phase in the electrode structure for sufficient electrocatalytic activity. This limitation causes increasing polarization resistance when using mixed P-RP electrodes under high reducing conditions. In our former work, the details of increasing the polarization resistance in a similar mixed P and RP electrode were discussed for the $Sr_{0.5}Pr_{0.5}MnO_3$.^[32] A complete P-to-RP transformation forms a blocking layer and causes a significant degradation in cell performance.

Compared to SPCM1, the higher concentration of Ce in SPCM2 stabilizes the perovskite structure under more reducing conditions, forming a mixed RP-P electrode and enhancing its

electrocatalytic activity toward surface reactions. This structural stability is a key factor contributing to the lower R_p observed for SPCM2 compared to SPCM1 in atmospheres containing 3–10% H_2O .

XPS analysis of the reduced powders reveals AOS of +3.35 for Pr and +3.8 for Ce, indicating that Ce substitution reduces the oxygen vacancy concentration in the SPCM structure. Additionally, higher steam partial pressures further decrease oxygen vacancy concentrations by increasing the oxidation states of the cations. Since oxygen vacancies are critical for ionic conductivity, this reduction leads to a steady increase in R_p for SPCM2 as steam partial pressure rises.

In contrast, the kinetic of the electrode reaction can be optimized at the high steam concentrations of 20–60% H_2O for the SPCM1 electrode when the oxygen vacancy concentration and kinetic of the surface reaction are sufficiently high. The complex electrode reactions coupled with dynamic conditions in phase evolution make identifying rate-limiting mechanisms challenging for electrodes with different Ce concentrations.

A similar trend was observed for the ohmic resistance, primarily due to the influence of gas compositions on oxygen vacancy concentration within the P structure and the mobility of oxygen ions through the interstitial sites within the RP structure.

Compared to SPCM2, although SPCM1 shows higher electrocatalytic activity at 40–60% $H_2O/(H_2O+H_2)$, operating this cell under high electrolysis current densities can lead to a high local hydrogen activity close to the electrode surface. An intense reducing condition at the electrode surface can quickly cause SPCM1 with lower Ce content to form a single RP phase. Consequently, the complete P-to-RP transformation can interrupt surface reaction, as reported for the single-phase RP electrode.^[32] Degradation of polarization resistance due to this phase evolution was also observed during the initial measurement in 3% $H_2O/(H_2O+H_2)$ at 800 °C for the SPCM1 electrode. We have therefore excluded the SPCM1 electrode from further investigation in full-cell configuration.

Figure 8 displays the typical impedance spectra and distributed relaxation time (DRT) plots for the SPCM2 electrode in a full-cell configuration containing LSCF perovskite as an air electrode. The impedance spectra were measured at 650–800 °C, and the gas composition at the fuel side was considered 3% and 60% $H_2O/(H_2O+H_2)$. Pure oxygen was utilized on the air side since no air purge is required for SOEC operating at thermoneutral conditions, and it prevents the gas diffusion process from contributing to the impedance data. The Nyquist plots represent the high electrocatalytic activity of the SPCM2 electrode toward the hydrogen reduction/oxidation above 700 °C. Accordingly, measured impedance spectra at 800 °C showed small R_p of 0.043 and 0.055 $\Omega\text{ cm}^2$ in 3% and 60% $H_2O/(H_2O+H_2)$, respectively.

The impedance spectra were analyzed using the distribution of relaxation times (DRT) to identify the processes contributing to the overall cell performance. DRT can deconvolute electrochemical reactions with close time constants for a detailed interpretation of electrochemical performance. Accordingly, the corresponding DRT plots are illustrated next to the Nyquist plots in **Figure 8**.

Through DRT analysis, a clear distinction of electrochemical processes at the measured frequency range (from 1MHz to 3mHz) and their contributions to the overall polarization

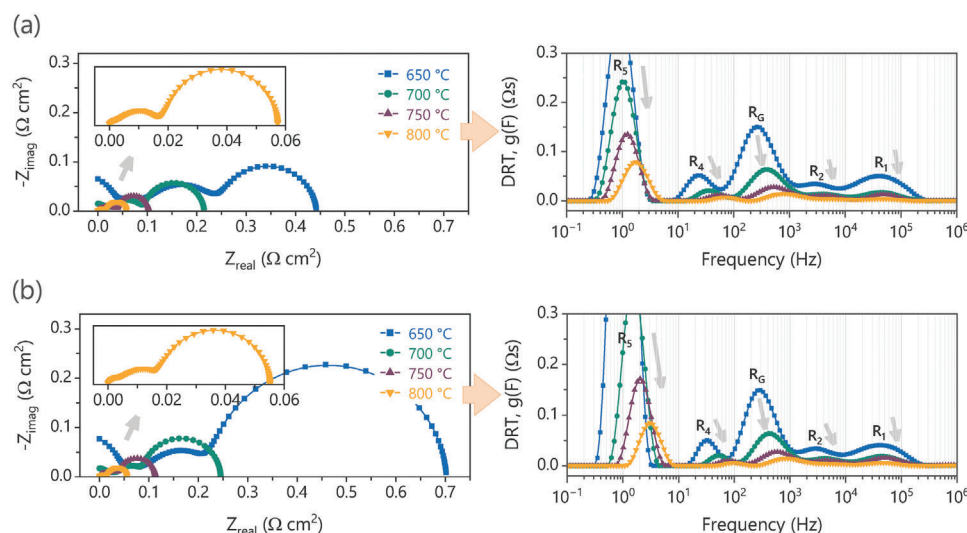


Figure 8. Temperature dependency of impedance spectra and corresponding DRT plots for the cell containing SPCM2 and LSCF electrodes in a) 3% $\text{H}_2\text{O}/(\text{H}_2\text{O}+\text{H}_2)$ and b) 60% $\text{H}_2\text{O}/(\text{H}_2\text{O}+\text{H}_2)$ gases. Note: pure oxygen is utilized on the air side to minimize gas diffusion resistance at low frequencies.

resistance can be observed. The DRTs were calculated using a Tikhonov regularization-based approach.^[60] This approach requires the regularization parameter (λ), which is the most critical parameter for the DRT calculation since it keeps the profile smooth and reduces the occurrence of artificial peaks.^[61] By selecting an optimal value of $\lambda = 0.005$, the number of individual processes with different relaxation frequencies has been identified to interpret the Nyquist plots. Accordingly, the overall impedance spectra show five peaks in the DRT: two high-frequency peaks (HF, $f > 10^3$ Hz), two middle-frequency peaks (MF, $f = 10\text{--}10^3$ Hz), and one low-frequency peak (LF, $f < 10$ Hz). By identifying these peaks in the DRT plots, the following equivalent circuit is considered for studying the impedance spectra for the SPCM2 electrode in a full-cell configuration.

$$R_{\Omega} (R_1 Q_1) (R_2 Q_2) R_G (R_4 Q_4) (R_5 Q_5) \quad (3)$$

The electrode reaction is complex, involving multiple steps, and is affected by gas composition (oxygen and steam partial pressure), cell processing techniques, sintering temperature, operational methods, and the phase stability of electrode material.^[62] Collectively, these factors make interpreting specific reactions within the impedance spectrum challenging.

As a first step in interpreting the fuel electrode reaction involved in hydrogen reduction/oxidation and transport processes, it is required to distinguish the reaction originating from the air electrode. Besides, minimizing the degradation mechanisms caused by the air electrode facilitates understanding the stability behavior of the subjected SPCM2 electrode. For this purpose, varying the p_{O_2} on the air side can help identify corresponding resistances to the LSCF electrode. Accordingly, the gas composition on the fuel side is kept constant at 3% $\text{H}_2\text{O}/(\text{H}_2\text{O}+\text{H}_2)$, and impedance spectra are measured at 750 °C while varying the oxygen partial pressure from $p_{\text{O}_2} = 0.02$ to 1 atm by mixing O_2 and N_2 gases.

Figure 9 shows the dependency of impedance spectra, DRTs, and sub-resistance values on the oxygen partial pressure and

obtained reaction orders (n) for the fit results. The DRT plots (Figure 9b) indicate relatively constant resistances for the HF- R_1 , HF- R_2 , and MF- R_4 reactions with a quite small reaction order (Figure 9c). At the same time, a high dependency on p_{O_2} has been recorded for the R_G at a middle frequency and R_5 resistance at a low frequency. Based on the literature, the coupled electrochemical surface reaction and oxygen ion diffusion in the air electrode can be described with a Gerischer element at 10^2 to 10^3 Hz range.^[63,64] It can be concluded that the MF- R_G with a reaction order of ($n = 0.12$) refers to the LSCF air electrode reaction. Polarization resistance and relaxation frequency range are in excellent agreement with previous studies on cells containing the same LSCF electrode.^[65]

As the reaction was most influenced by p_{O_2} , the LF-(R_5 & R_6) showed a resistance drop ($n = 1$) with increasing oxygen partial pressure from 0.02 to 0.2 atm (a similar O_2 and N_2 mixture in the air). This is the characteristic feature of gas diffusion resistance reported for the air electrode with a perovskite structure, and its resistance dependency follows the equation below.^[23,65,66]

$$R_D (\text{air electrode}) \propto \frac{1}{p_{\text{O}_2}} - 1 \quad (4)$$

According to the above equation, further increasing the p_{O_2} to 1 by utilizing pure oxygen on the air side must suppress the gas diffusion resistance to zero. However, the obtained results demonstrate polarization of $0.069 \Omega \text{ cm}^2$ for LF-(R_5 & R_6) in $p_{\text{O}_2} = 1$. Moreover, the study of LF-(R_5 & R_6) dependency on the fuel gas composition represented decreasing polarization resistance for this reaction with hydrogen partial pressure (it is provided in the following, called LF- R_5). It can be concluded that two resistances with very close relaxation frequencies are present at low frequencies (LF, $f < 10$ Hz), which makes it impossible to distinguish them using the DRT. Accordingly, we have used pure oxygen on the air side to eliminate the contribution of gas diffusion resistance in our interpretation of low-frequency resistance. From now on, the LF-(R_5 & R_6) will be replaced by

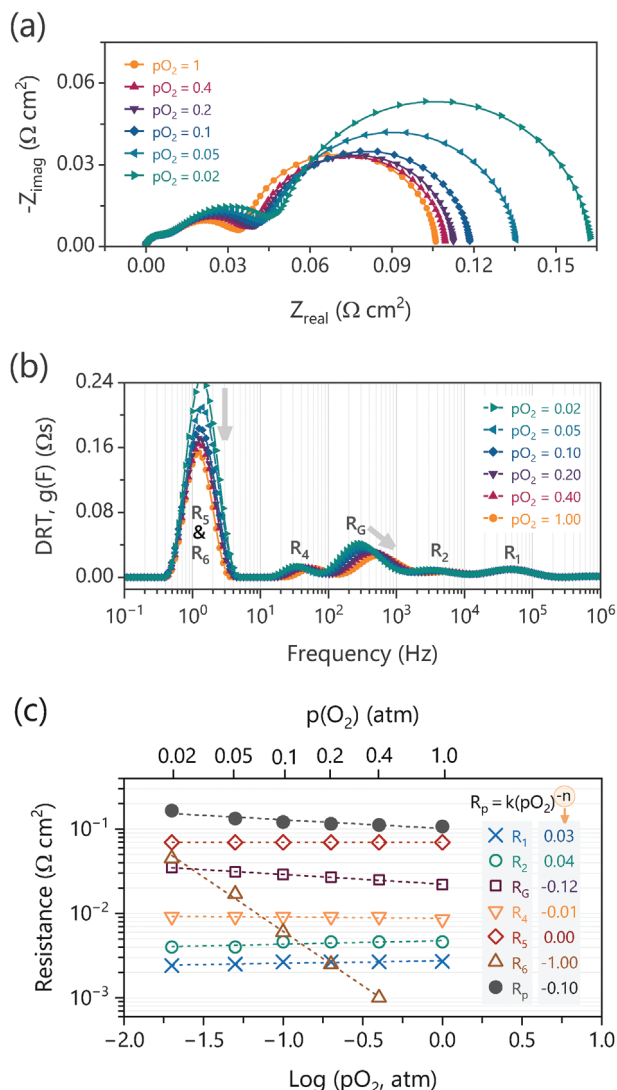


Figure 9. Oxygen partial pressure dependency of a) impedance spectra, b) corresponding DRTs, and c) the fitted polarization processes of the cell containing SPCM2 and LSCF electrodes at 750 °C. (Note: the gas composition for the fuel side was kept constant at 3% H₂O/(H₂O+H₂)).

LF-R₅ since the polarization resistance for LF-R₆ is supposed to be zero using pure oxygen on the air side.

Following identifying the resistances originating from the LSCF air electrode, we will analyze the impedance spectra and discuss the influence of the operation conditions by fitting an equivalent circuit model (ECM). In order to interpret physicochemical reactions in impedance spectra as combined complex electrochemical processes, temperature and steam partial pressures on the fuel side are varied to determine the characteristic features of the processes. Varying these operating parameters provides information about the physicochemical background of DRT peaks in hydrogen reduction/oxidation reactions.^[67] It needs to be noted that a variation in steam partial pressure is closely associated with a variation in the RP/P ratio in the SPCM electrode, which may significantly accelerate or diminish the reaction kinetics. Therefore, the possibility of P-to-RP phase trans-

formation under different p_{H₂O} can complicate the interpretation of impedance spectra for hydrogen reduction/oxidation reactions.

Figure 10a,b display the Nyquist and corresponding DRT plots in 60% H₂O/(H₂O+H₂) at 800 °C. In addition, **Figure 10c,d** provide the temperature and steam concentration dependency of the sub-polarization resistances, respectively. In fitted resistances, minor high-frequency peaks (HF-R₁ and HF-R₂ resistances) with a high activation energy of 2.06–2.34 eV were observed in the DRT plots, indicating a minimal contribution of these resistances to the overall polarization resistance.

According to the equation below, the calculated capacitance for HF-R₁ and HF-R₂ resistances indicates a small capacitance of C₁ = 0.001 and C₂ = 0.040 F cm⁻².

$$C \text{ (Fcm}^{-2}\text{)} = R^{(1/n)-1} Q^{1/n} \quad (5)$$

The reactions with a small capacitance are typically associated with rapid interfacial processes, such as charge transfer or transport process at a solid/solid interface,^[19] which in our case is the SPCM/CGO, LSCF/CGO, or the CGO/YSZ interfaces.^[2] **Figure 9c** illustrated neglectable reaction orders (n₁ = 0.03 and n₂ = 0.04) with varying oxygen partial pressures in synthetic air based on the slope of fitted lines for the HF-R₁ and HF-R₂ resistances. When steam partial pressure is varied on the fuel side (**Figure 10d**), HF-R₁ shows an increase in reaction order to n₁ = 0.10, while N₂ remains at the same magnitude, i.e., 0.02. It is reported that the interfacial processes are strongly affected by the chemistry of interlayers,^[68] and even minor changes in material composition or processing parameters can result in significant variations of the related resistances.^[69] The possibility of changes in the oxidation state of the cations for both CGO fluoride and SPCM perovskite structures under reducing conditions and, consequently, decreasing the oxygen vacancy concentration can be the probable explanation for the slight increase in the resistance of HF-R₁ reaction with steam partial pressure. On the other hand, the HF-R₂ resistance is most likely related to the interfacial YSZ/CGO and LSCF/CGO process on the air side. Nevertheless, the close relaxation frequencies of the charge transfer and transport processes in the air and fuel electrodes overlap the corresponding semicircles in the Nyquist plot, making it difficult to distinguish between them accurately.

The ECM fitting results at middle frequencies show two MF-R_C and MF-R₄ resistances. As discussed earlier, the third resistance (MF-R_C) is fitted by the Gerischer element describing the electrochemical reaction on the air side, which includes coupled surface oxygen dissociation and oxygen ion diffusion through the LSCF grains. Due to the constant partial pressure of oxygen on the air side when using pure oxygen, the reaction order of zero was measured at 800 °C (**Figure 10d**), which reveals a constant resistance of MF-R_C = 0.012 Ω cm² in different steam partial pressures.

The fitting results show accelerated reaction kinetics in the investigated gas compositions for the MF-R₄ process with a negative reaction order between -0.03 and -0.10 (**Figure 10d**). Similarly, the LF-R₅ process with an apparent activation energy of 1.46 eV shows a negative reaction order (n = -0.1) at a steam range of 3–20% H₂O/(H₂O+H₂), while the corresponding resistance increases with steam partial pressure above 20% H₂O/(H₂O+H₂).

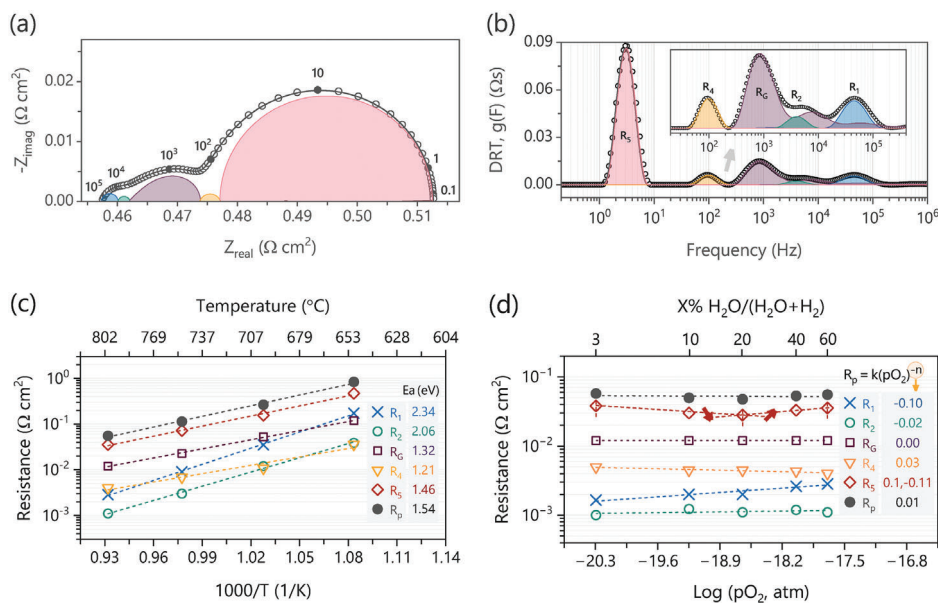
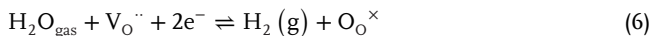


Figure 10. a) the Nyquist spectrum, b) corresponding DRT plots along with fitted sub-polarization resistances for the cell containing SPCM2 and LSCF electrodes, c) Arrhenius plots of fitted resistances in 60% H₂O/(H₂O+H₂), and d) steam partial pressure dependency of sub-polarization resistances at 800 °C. Note: The steam partial pressure varies in (d), whereas pure oxygen is utilized on the air side, which leads to identical MF-R₄ resistance attributed to the LSCF electrode.

The *n* values for all testing temperatures are provided in Figure 7s (Supporting Information). Variation of the MF-R₄ and LF-R₅ peaks in DRT plots to the steam partial pressure suggests that these reactions are related to the electrochemical reaction in the SPCM2 electrode. The fitted ECM for the MF-R₄ represents a high activation energy of *E*_{a4} = 1.11-1.35 eV and capacitance of *C*₄ = 0.45-0.61 F cm⁻², and corresponding values for the LF-R₅ resistance are *E*_{a5} = 0.91-1.46 eV and *C*₅ = 1.50-2.46 F cm⁻².

Interpreting the MF-R₄ and LF-R₅ resistances requires looking at the physiochemical reactions involved in hydrogen oxidation/reduction. Accordingly, the overall reaction in steam electrolysis can be presented as follows^[70]:

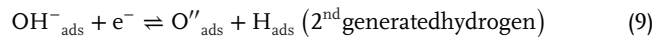
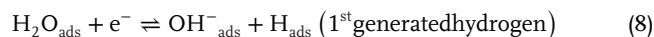


According to the Kröger-Vink notation, the V_O^{··} and O_O[×] denote an oxygen vacancy and regular lattice oxygen in the perovskite/Ruddlesden-Popper structure, respectively. The MIEC electrode enables this reaction by conducting the oxygen ions (O²⁻) and electrons (e⁻) simultaneously on the electrode surface. Accordingly, the main steps involved in the steam electrolysis reaction can be described as the adsorption of the steam molecule, surface charge transfer reaction, and incorporation of oxygen into the electrode structure.^[32,71] These processes are chemisorption reactions on the SPCM grain's surface, where an oxygen vacancy is preferably at the reaction site.



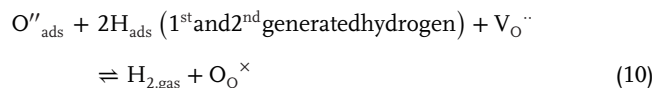
Following the adsorption reaction of H₂O on the SPCM surface (Equation 7), the adsorbed steam can dissociate into its constituent ions. It involves breaking steam chemical bonds to hy-

droxide ions (OH⁻_{ads}) and later to hydrogen (H_{ads}) by getting electrons in two steps through the SPCM backbone.^[71-73]



The oxidation of H₂O_{ads} by transferring the electron at the electrode/gas interface through (Equations 8 and 9) has been assessed to be the principal MIEC surface charge transfer reaction for H₂ oxidation and H₂O electrolysis,^[32] forming physically bonded hydrogen atoms on the SPCM grain's surface.

Finally, the hydrogen gas is formed by combining hydrogen atoms followed by desorption.



The continued dissociative adsorption of steam molecules would only be possible if the oxide ion's mobility in the SPCM structure were high enough. Accordingly, the diffusion of the oxide ions (O²⁻) from the electrocatalytic active surface sites to the electrode/electrolyte interface can lead to another resistance, which is reported with a much higher capacitance compared to double-layer capacitance (HF-R₁ and HF-R₂) in the MIEC fuel electrode.^[32]

The complexity of the hydrogen oxidation/reduction reaction and the possibility of P-to-RP phase transformation makes it difficult to distinguish the reactions described above in Nyquist spectra. Moreover, the deviation of fitted resistance for LF-R₅ from linear behavior (Figure 10d) reveals the dependency of characteristics of the SPCM electrode on the gas composition, as similar behavior has also been reported for other MIEC electrode

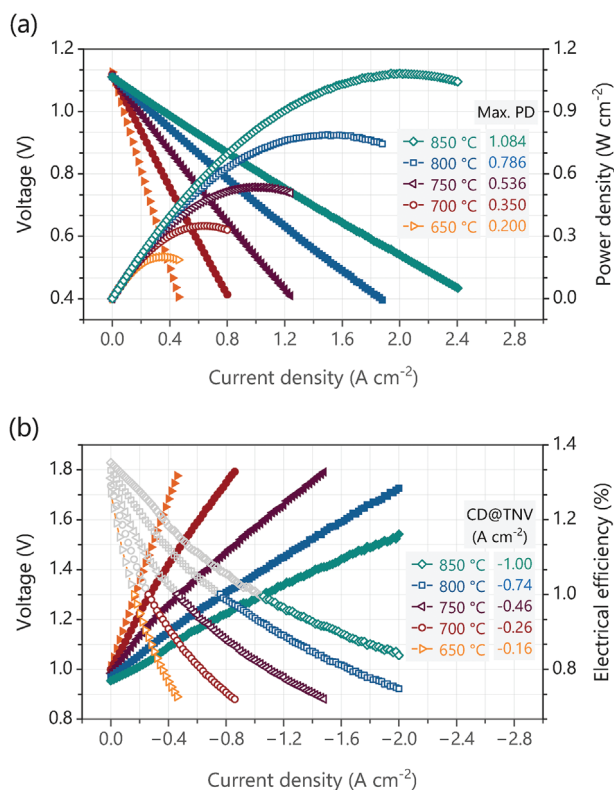


Figure 11. I-V characteristic of the cell containing SPCM2 and LSCF electrodes for a) fuel cell (FC) operation mode in 3% H₂O/(H₂O+H₂) and b) electrolysis cell (EC) operation mode in 50% H₂O/(H₂O+H₂).

materials.^[32,74] However, it can be concluded that thermally activated LF-R₅ resistance with relative dependency to the steam partial pressure is most likely related to the surface reactions, and MF-R₄ with a higher capacitance compared to HF resistances is related to oxygen ions diffusion through the SPCM2 bulk.

Figure 11 shows the I-V characteristic of the SPCM electrode in a full-cell configuration containing the LSCF air electrode. Although the prepared electrolyte-supported cell hinders obtaining the optimum performance below 800 °C due to its high ohmic resistance, evaluating power output at higher temperatures can provide insight to be considered for commercial ESCs. Accordingly, the measurement was conducted in the FC mode operation using 3% H₂O/(H₂O+H₂) and EC mode operation using 50% H₂O/(H₂O+H₂) at 650–850 °C temperature range. The open circuit voltages (OCVs) in the FC and EC operation conditions were recorded at 1.11 ± 0.01 V and 0.97 ± 0.02 V, respectively. These values are close to the calculated based on the Nernst equation (OCV_{th,FC} = 1.131 V and OCV_{th,EC} = 0.963 V),^[75,76] and indicate negligible gas leakage and deviations in flow rates in the test setup as well as no electronic leakage through the dense 3YSZ electrolyte.

$$OCV_{th} = \frac{RT}{2F} \ln \frac{\sqrt{PO_2, \text{ air electrode}}}{\sqrt{PO_2, \text{ fuel electrode}}} \quad (11)$$

The FC operation was carried out between the OCV and 0.4 V, and pure oxygen was utilized on the air side to avoid oxygen

starving at high current densities, which can cause degradation of the LSCF electrode. The maximum power density reached 0.786 and 1.084 W cm⁻² at 800 and 850 °C, respectively (Figure 11a). These values are remarkably higher than those obtained previously for perovskites like STFMs (0.573 W cm⁻² at 850 °C, 0.444 W cm⁻² at 800 °C),^[77] SFM (0.650 W cm⁻² at 850 °C, 0.500 W cm⁻² at 800 °C),^[78] and AFM (A = Ca, Sr, Ba) series (0.757 W cm⁻² at 850 °C, 0.614 W cm⁻² at 800 °C).^[79] The generated high power densities with comparable values to those obtained for Ni cermet electrodes (0.7–0.73 W cm⁻² at 800 °C)^[80,81] indicate the capability of the SPCM2 as a Ni-free electrode to operate in SOFC conditions.

When considering the technical application of SPCM2 cells in an SOFC operation mode, it is crucial to consider that at maximum power, the cell voltage falls below 600 mV, which results in a relatively low electrical efficiency. Operating voltages between 700 and 850 mV are more reasonable, resulting in power densities of 0.971 W cm⁻² at 0.7 V and 850 °C.

The voltage response of the investigated cell under EC operation was measured in 50% H₂O/(H₂O+H₂) with a limited maximum voltage of 1.8 V and a maximum current density of -2.0 A cm⁻². Similar to the FC measurements, the air electrode is operated in pure oxygen. It should be noted that pure oxygen enhances the FC performance, but it also has a negative impact on the EC performance. Figure 11b shows IV characteristics and electrical efficiency versus current density in the 650–850 °C range. Unlike the fuel cell mode, the voltage continuously increases with applying current due to the internal resistance. For this reason, a maximum power density can not be given in EC operation. Instead, the most common reference parameter is the current density value at a thermoneutral voltage (TNV) for high-temperature electrolysis (V_{TNV} = 1.29 V).^[82]

The utilized 3YSZ electrolyte with a thickness of 40 μm in this work is a recently developed benchmark electrolyte to improve the electrochemical performance of ESCs. As a result, decreased ohmic resistance makes I-V characteristic comparison difficult to those reported in the literature with thicker electrolytes. At the same time, the 40 μm electrolyte is much thicker than the electrolyte in the fuel electrode-supported cells. Nevertheless, the operating investigated ESC cell under thermoneutral voltage represents high current densities of -0.74 A cm⁻² at 800 °C. This is reasonably higher than recently reported values for the most promising Ni-CGO (I_{@TNV} = -0.5 A cm⁻² at 800 °C)^[83] and 3Mo-3Au-Ni-CGO (I_{@TNV} = -0.361 A cm⁻² at 800 °C)^[84] electrodes in ESC configuration.

In addition, electrical efficiency can be calculated by dividing the TNV by the cell voltage at the applied current density,^[70] which leads to an electrical efficiency higher than 100% below TNV due to the effect of thermal energy on steam electrolysis. The obtained cell potential (1.39 V) at 800 °C is still small enough to achieve a high current density of 1.00 A cm⁻² to keep electrical efficiency above 93% in hydrogen production, which is of great interest in commercial applications.

Finally, the durability study was carried out for 350 h under initially thermoneutral conditions (I = -0.74 A cm⁻²) at 800 °C using 60% H₂O/(H₂O+H₂) on the fuel side and synthetic air on the air side for steam electrolysis. Accordingly, the ESC cell was operated under a galvanostatic mode, and impedance spectra were measured under current and OCV conditions every six hours.

Since the reaction kinetic highly changes under applied current, the impedance spectra under OCV conditions are considered for comparison with the initially measured data. The overview of the variation of R_{Ω} , R_p , and overpotential is shown in Figure 8s (Supporting Information).

The results calculated a minor degradation rate of 0.02 and 0.06 $\Omega \text{ cm}^2 \text{ kh}^{-1}$ for R_{Ω} and R_p resistances, respectively. Moreover, the stability of cell performance under thermoneutral conditions shows an increase in the over-potential at a 45 mV kh^{-1} rate. This degradation rate is quite low compared to the other reported data in the literature for Ni-YSZ or Ni-CGO electrodes in single cells. For instance, Sciazko et al. have recently compared the degradation behavior of Ni-YSZ and Ni-CGO electrodes under a current density of -0.2 A cm^{-2} for steam electrolysis at 800 °C.^[85] Although a better initial performance was observed for the Ni-CGO electrode, cell voltages were increased by ≈ 180 and 120 mV for Ni-CGO and Ni-YSZ electrodes after 100 h. A significantly lower degradation rate for SPCM2|3YSZ|LSCF cell demonstrates its potential to be considered for further investigation taking into commercial applications.

3. Conclusion

The sol-gel combustion method was successfully employed to synthesize a series of $\text{Sr}_{0.6}\text{Pr}_{0.4-x}\text{Ce}_x\text{MnO}_3$ (SPCM) perovskites with varying Ce concentrations ($x = 0.1, 0.2, 0.3$). The evaluation of phases under SOC operation conditions reveals the forming of mixed perovskite and Ruddlesden-Popper structures at 600–800 °C. The investigation of A-site substitution by Ce cations demonstrated that increasing Ce concentration intensifies the formation of the $\text{Ce}_{0.5}\text{Pr}_{0.5}\text{O}_2$ (CPO) phase, which causes the decomposition of the perovskite phase under a reducing atmosphere for the $x = 0.3$. Meanwhile, phase transformation to Ruddlesden-Popper was observed for lower substitution concentrations ($x = 0.1$ and 0.2). According to the Rietveld refinement, the b and c crystal parameters in the perovskite with an orthorhombic structure (Imma (74) space group, $a = 5.494 \text{ \AA}$, $b = 7.569 \text{ \AA}$, and $c = 5.585 \text{ \AA}$) increase with temperature. In contrast, the “a” parameter reaches its minimum value of 5.475 Å at 650 °C. Further increasing temperature above 650 °C led to perovskite-to-Ruddlesden Popper (P-to-RP) transformation with a tetragonal structure I4/mmm (139) and crystal parameters of $a = 3.836 \text{ \AA}$ and $c = 13.020 \text{ \AA}$.

The electrochemical performance of developed SPCM fuel electrodes was investigated in a 3YSZ electrolyte-supported cell and wide pH_2O range, i.e., 3–60% $\text{H}_2\text{O}/(\text{H}_2\text{O}+\text{H}_2)$. The study of impedance spectra for the symmetric cell showed performance degradation with hydrogen partial pressures for SPCM with lower Ce concentrations ($x = 0.1$). Increasing the R_p is mainly due to the significant increase in the RP/P ratio and poor electrocatalytic activity of the Ruddlesden-Popper toward hydrogen oxidation/reduction.

The Nyquist spectra analysis of the full cell revealed a small polarization resistance of $\text{MF-R}_C = 0.012 \text{ \Omega cm}^2$ for the air electrode, demonstrating that sintering the state-of-the-art LSCF electrode at 1080 °C produced a well-bonded layer to the electrolyte, ensuring high electrochemical surface activity and oxide ion conductivity in pure oxygen.

Additionally, four resistances corresponding to the fuel electrode reactions are identified in the impedance spectra. Two minor high-frequency resistances (HF-R_1 and HF-R_2) were attributed to the charge transfer and ionic transport at the SPCM/CGO, LSCF/CGO, and CGO/YSZ interfaces, reflecting no resistive intermediate phase formation and optimum processing conditions that produce well-bonded layers. A small middle-frequency resistance (MF-R_4) of $R_4 = 0.0045 \pm 0.0005 \text{ \Omega cm}^2$ at 800 °C, characterized by a higher capacitance than HF-resistances, likely corresponds to oxide ion diffusion through SPCM bulk. The reduced resistance at the middle frequency can be attributed to the enhanced electrode conductivity through the RP structure with a high concentration of mobile oxygen atoms, ensuring the excellent conductivity required for high-temperature SOC applications. On the other hand, at low frequency (LF-R_5), a small resistance ($0.033 \pm 0.005 \text{ \Omega cm}^2$) associated with hydroxide dissociation or evolution reactions was observed, demonstrating enhanced kinetic of surface reactions in 60% $\text{H}_2\text{O}/(\text{H}_2\text{O}+\text{H}_2)$ at 800 °C.

Despite using the 3YSZ electrolyte-supported cell with 40 μm thickness, the voltage response at different current densities revealed a high power density of 1.084 W cm^{-2} in FC mode and a current density of 1.00 A cm^{-2} at the thermoneutral voltage at 850 °C. Moreover, the stability analysis demonstrated a low overpotential degradation rate of 45 mV kh^{-1} , highlighting the potential of SPCM electrodes to be introduced as a very promising Ni-free candidate. Accordingly, it is necessary to investigate its durability for long-term industrial operation and optimize the processing parameters for implementing the SPCM electrode into SOC stacks.

4. Experimental Section

Powder Synthesis: The series of $\text{Sr}_{0.6}\text{Pr}_{0.4-x}\text{Ce}_x\text{MnO}_3$ (SPCM) ($x = 0.1, 0.2, 0.3$) perovskite were synthesized using the sol-gel combustion method. The samples are referenced as SPCM1, SPCM2, and SPCM3 for $x = 0.1, 0.2$, and 0.3 , respectively. Accordingly, for each perovskite composition, the stoichiometric amounts of nitrate precursors, including $\text{Pr}(\text{NO}_3)_3 \cdot 6\text{H}_2\text{O}$, $\text{Sr}(\text{NO}_3)_2$, $\text{Ce}(\text{NO}_3)_3 \cdot 6\text{H}_2\text{O}$, and $\text{Mn}(\text{NO}_3)_2 \cdot 4\text{H}_2\text{O}$ were dissolved in aquas citric acid ($\text{C}_6\text{H}_8\text{O}_7$) solution. The ratio of 1:1.5 for metal ions and citric acid is considered for optimized combustion reaction.^[34] The obtained sol was stirred for 2 h at 70 °C to achieve a transparent aqueous solution. Following this, the pH of the solution was adjusted to approximately neutral ($\text{pH} = 6.5\text{--}7.0$) by adding ammonia solution dropwise. Afterward, the viscous gel was obtained by heating the sol at 80 °C overnight, when more than 90% of the water content was removed. The gel was then heat treated at 350 °C for 1 h (with a heating rate of 5 °C min^{-1}). Accordingly, during the heat treatment, redox reactions occurred between carboxyl groups and nitrates, forming a foamy black ash.^[33,36] Afterward, the obtained black ash was further calcined in air at 800 °C (held for 3 h, with a heating and cooling rate of 3 °C min^{-1}) to yield the perovskite with the submicron-size powder. Furthermore, after calcination in air at 800 °C, the powder was heat treated at 600–800 °C under a reducing atmosphere (humidified 5% H_2/N_2) to investigate phase transformation under the SOC operation condition. In addition, the phase evolution was further investigated using in-situ XRD up to 850 °C to understand the P-to-RP transformation mechanism under a similar steam electrolysis condition.

Cell Preparation: For the preparation of symmetric and full cells, a $\text{Gd}_{0.2}\text{Ce}_{0.8}\text{O}_{2-\delta}$ (CGO) layer with a thickness of 5 μm was first screen printed on both sides of a 3YSZ electrolyte substrate (Kerafol, Keramische Folien GmbH & Co.) with a thickness of 40 μm . The CGO layer

operates as a barrier layer, inhibiting the formation of an insulating SrZrO₃ phase at the electrode/electrolyte interface.^[87,88] The screen printing was conducted separately for each side, followed by drying for 24 h at 70 °C. The CGO layers were sintered at 1300 °C for 3 h, beginning with a heating rate of 0.3 °C min⁻¹ from 25 to 500 °C (called a debinding step), then increasing to 1 °C min⁻¹. The slow heating rate from 25 to 500 °C avoids cracks and defects in the CGO layer, primarily caused by gas released from the decomposition of organic binders. Furthermore, this heating process promotes uniform and effective particle bonding, forming a denser barrier layer close to the electrolyte.

The fuel electrode ink for screen printing was prepared by mixing SPCM powder with various additives. The prepared SPCM slurry was then applied to the top of the CGO layer. The precursor materials for ink preparation were subjected to ball milling at 150 rpm for 8 h using a planetary ball mill. Dipropylglycol (DPG), poly (methylmethacrylate) (PMMA), sanitizer 261A, polyvinylpyrrolidone (PVP) K30, and PVP K90 were added as the solvent, pore-forming agent, plasticizer, dispersant, and binder, respectively. The amount of PMMA pore-forming is determined by 10 wt.% of total polymer loading to ensure adequate porosity. The symmetric cells containing SPCM electrodes on both electrolyte sides were sintered at 1200 °C for 3 h in the air, following the debinding step and heating rate of 1 °C min⁻¹ from 500 °C.

The solid oxide cell in a full-cell configuration was prepared by prior sintering the SPCM fuel electrode, screen printing the LSCF air electrode, and performing the second sintering cycle. In this regard, the air electrode ink is prepared by mixing the additives, including Terpinol, Ethylcellulose, Dictylphthalat, and Thixatrol ST, and then adding the LSCF powder at 60 °C to reach 60% of solid loading. Further details on LSCF electrode processing and its electrochemical properties are provided in the former publication.^[65,89] Finally, the air electrode was sintered at 1080 °C for 3 h in the air, with a similar debinding step and rate to the fuel electrodes.

Last, the gold layer was also screen-printed on the SPCM electrode and sintered during electrochemical testing to ensure electrical connections to the external circuit.

Characterization and Electrochemical Testing: The crystal structure and phase evolution of SPCM powder were characterized by X-ray diffraction at room temperature and in-situ mode in the 2θ range of 10°–90° (Bruker D8 Advance diffractometer with Cu Kα radiation (λ = 1.54 Å^[42]). The Rietveld refinement was performed using FullProf Suite software on the powder samples heat-treated in both air and reducing atmosphere (5% H₂/N₂, with pO₂ = 1.86 × 10⁻²² atm at 800 °C). This refinement process aided in further studying the lattice parameters, space groups, occupation of the crystal sites, and secondary phases in prepared oxide. Moreover, an analysis of the oxidation state of cations in the SPCM oxide with perovskite and Ruddlesden-Popper structures was carried out by XPS (Thermo Scientific, ESCALAB XI⁺) using an Al Kα radiation monochromatic source.

Scanning electron microscopy (Zeiss CrossBeam XB 1540) equipped with an energy dispersive spectrometer (EDS) was employed to investigate the microstructure and distribution of porosity in the LSCF and SPCM electrodes as well as identify the thickness of applied layers in the symmetric and full-cells.

The electrochemical performance was evaluated through I-V curves and electrochemical impedance spectroscopy (EIS) at open-circuit voltage (OCV). The steam partial pressure was set from 3% H₂O to 60% H₂O. Details on the applied test bench and testing methodologies can be found in.^[90] Accordingly, the distribution of relaxation times (DRT) was employed to identify the number of processes involved in hydrogen oxidation/reduction reactions and study the polarization resistance and characteristic frequency ranges for each process. Subsequently, the complex nonlinear least square (CNLS) fitting was used to create an equivalent circuit model to interpret individual physical and electrochemical processes in impedance data.

Supporting Information

Supporting Information is available from the Wiley Online Library or from the author.

Acknowledgements

The authors gratefully acknowledge funding from the Federal Ministry of Education and Research (BMBF 03SF0621G). In addition, the authors would like to express their appreciation to Annette Schucker for her technical assistance with SEM microscopy at KIT (IAM-ET).

Conflict of Interest

The authors declare no conflict of interest.

Data Availability Statement

The data that support the findings of this study are available from the corresponding author upon reasonable request.

Keywords

electrochemical impedance spectroscopy, material synthesis, phase evolution, Power-to-X, steam electrolysis

Received: October 18, 2024

Revised: December 15, 2024

Published online:

- [1] D. M. A. Dueñas, M. Riedel, M. Riegraf, R. Costa, K. A. Friedrich, *Chemie Ing. Tech.* **2020**, *92*, 45.
- [2] Y. Alizad Farzin, A. Babaei, T. Løye Skafte, E. Stamate, A. Ataie, S. H. Jensen, *Int. J. Hydrogen Energy* **2022**, *47*, 7915.
- [3] S. H. Jensen, P. H. Larsen, M. Mogensen, *Int. J. Hydrogen Energy* **2007**, *32*, 3253.
- [4] C. Graves, S. D. Ebbesen, M. Mogensen, *Solid State Ionics* **2011**, *192*, 398.
- [5] M. S. Khan, S. B. Lee, R. H. Song, J. W. Lee, T. H. Lim, S. J. Park, *Ceram. Int.* **2016**, *42*, 35.
- [6] M. Chen, Y.-L. Liu, J. J. Bentzen, W. Zhang, X. Sun, A. Hauch, Y. Tao, J. R. Bowen, P. V. Hendriksen, *J. Electrochem. Soc.* **2013**, *160*, F883.
- [7] A. Žužić, A. Ressler, J. Macan, *Ceram. Int.* **2022**, *48*, 27240.
- [8] S. Vasala, M. Karppinen, *Prog. Solid State Chem.* **2015**, *43*, 1.
- [9] H. Lv, Y. Zhou, X. Zhang, Y. Song, Q. Liu, G. Wang, X. Bao, *J. Energy Chem.* **2019**, *35*, 71.
- [10] J. T. S. Irvine, D. Neagu, M. C. Verbraeken, C. Chatzichristodoulou, C. Graves, M. B. Mogensen, *Nat. Energy* **2016**, *1*, 15014.
- [11] P. Li, Y. Han, M. Xu, T. Jin, F. Yan, T. Gan, R. Wang, *Energy and Fuels* **2022**, *36*, 15165.
- [12] H. Lv, T. Liu, X. Zhang, Y. Song, H. Matsumoto, N. Ta, C. Zeng, G. Wang, X. Bao, *Angew. Chem., Int. Ed.* **2020**, *59*, 15968.
- [13] D. M. Amaya-Dueñas, M. Riegraf, A. Nanning, A. K. Opitz, R. Costa, K. A. Friedrich, *ACS Appl. Energy Mater.* **2022**, *5*, 8143.
- [14] D. Neagu, T. S. Oh, D. N. Miller, H. Ménard, S. M. Bukhari, S. R. Gamble, R. J. Gorte, J. M. Vohs, J. T. S. Irvine, *Nat. Commun.* **2015**, *6*, 8120.
- [15] Q. Yang, H. Wu, K. Song, B. A. Beshiwork, X. Luo, D. Tian, S. Zhu, X. Lu, Y. Ding, Y. Chen, B. Lin, *Ceram. Int.* **2022**, *48*, 31418.
- [16] L. Duranti, I. Natali Sora, F. Zurlo, I. Luisetto, S. Licoccia, E. Di Bartolomeo, *J. Eur. Ceram. Soc.* **2020**, *40*, 4076.
- [17] T. Ma, T. Xia, Q. Li, L. Sun, L. Huo, H. Zhao, *J. Eur. Ceram. Soc.* **2022**, *42*, 490.
- [18] S. Zhou, Y. Yang, H. Chen, Y. Ling, *Ceram. Int.* **2020**, *46*, 18331.
- [19] Z. Du, H. Zhao, S. Yi, Q. Xia, Y. Gong, Y. Zhang, X. Cheng, Y. Li, L. Gu, K. Świerczek, *ACS Nano* **2016**, *10*, 8660.

- [20] C. Y. Tsai, C. M. McGilvery, A. Aguadero, S. J. Skinner, *Int. J. Hydrogen Energy*. **2019**, *44*, 31458.
- [21] X. Tong, F. Zhou, S. Yang, S. Zhong, M. Wei, Y. Liu, *Ceram. Int.* **2017**, *43*, 10927.
- [22] Z. Han, J. Bai, X. Chen, X. Zhu, D. Zhou, *Int. J. Hydrogen Energy*. **2021**, *46*, 11894.
- [23] Y. Alizad Farzin, M. Harenbrock, D. Nardini, A. Weber, *Solid State Ionics* **2024**, *411*, 116569.
- [24] J. Zhang, C. Lenser, N. Russner, A. Weber, N. H. Menzler, O. Guillon, *J. Am. Ceram. Soc.* **2023**, *106*, 93.
- [25] S. Sengodan, S. Choi, A. Jun, T. H. Shin, Y. W. Ju, H. Y. Jeong, J. Shin, J. T. S. Irvine, G. Kim, *Nat. Mater.* **2015**, *14*, 205.
- [26] M. V. Sandoval, C. Cárdenas, E. Capoen, C. Pirovano, P. Roussel, G. H. Gauthier, *Electrochim. Acta.* **2019**, *304*, 415.
- [27] S. Yoo, S. Choi, J. Kim, J. Shin, G. Kim, *Electrochim. Acta.* **2013**, *100*, 44.
- [28] J.-H. Kim, F. Prado, A. Manthiram, *J. Electrochem. Soc.* **2008**, *155*, B1023.
- [29] M. V. Sandoval, C. Cardenas, E. Capoen, P. Roussel, C. Pirovano, G. H. Gauthier, *Electrochim. Acta.* **2020**, *353*, 136494.
- [30] Y. S. Chung, T. Kim, T. H. Shin, H. Yoon, S. Park, N. M. Sammes, W. B. Kim, J. S. Chung, *J. Mater. Chem. A.* **2017**, *5*, 6437.
- [31] K. J. Kim, M. K. Rath, H. H. Kwak, H. J. Kim, J. W. Han, S. T. Hong, K. T. Lee, *ACS Catal.* **2019**, *9*, 1172.
- [32] Y. Alizad Farzin, M. Bjerg Mogensen, S. Pirou, H. Lund Frandsen, *J. Power Sources*. **2023**, *580*, 233450.
- [33] Y. Alizad Farzin, O. Mirzaee, A. Ghasemi, *Mater. Chem. Phys.* **2016**, *178*, 149.
- [34] Y. A. Farzin, A. Babaei, A. Ataie, *Ceram. Int.* **2020**, *46*, 16867.
- [35] E. Hosseinkhan Nejad, Y. A. Farzin, M. A. Heydari, *J. Magn. Magn. Mater.* **2017**, *423*, 226.
- [36] R. RAN, X. WU, C. QUAN, D. WENG, *Solid State Ionics* **2005**, *176*, 965.
- [37] M. Khazaei, A. Malekzadeh, F. Amini, Y. Mortazavi, A. Khodadadi, *Cryst. Res. Technol.* **2010**, *45*, 1064.
- [38] F. Deganello, G. Marci, G. Deganello, *J. Eur. Ceram. Soc.* **2009**, *29*, 439.
- [39] I. Bretos, R. Jiménez, M. L. Calzada, M. K. Van Bael, A. Hardy, D. Van Genechten, J. Mullens, *Chem. Mater.* **2006**, *18*, 6448.
- [40] M. Gupta, P. Yadav, W. Khan, A. Azam, A. H. Naqvi, R. K. Kotnala, *Res. Artic. Adv. Mat. Lett.* **2002**, *2012*, 220.
- [41] A. Aliasgharzadeh-Polesangi, H. Abdollah-Pour, Y. A. Farzin, *J. Mater. Res. Technol.* **2019**, *8*, 1014.
- [42] O. Mirzaee, R. Mohamady, A. Ghasemi, Y. A. Farzin, *Int. J. Mod. Phys. B.* **2015**, *29*, 1550090.
- [43] P. Ding, W. Li, H. Zhao, C. Wu, L. Zhao, B. Dong, S. Wang, *JPhys Mater* **2021**, *4*, 022002.
- [44] E. Lay, G. Gauthier, L. Dessemond, *Solid State Ionics* **2011**, *189*, 91.
- [45] R. D. Shannon, *Acta Crystallogr. Sect. A.* **1976**, *32*, 751.
- [46] H. Kim, C. Lim, O. Kwon, J. Oh, M. T. Curnan, H. Y. Jeong, S. Choi, J. W. Han, G. Kim, *Nat. Commun.* **2021**, *12*, 6814.
- [47] P. Leuaa, Y. A. Farzin, S. Iqbal, C. Chatzichristodoulou, *J. Power Sources*. **2025**, *625*, 235625.
- [48] S. Chen, Y. Hao, R. Chen, Z. Su, T. Chen, *J. Alloys Compd.* **2021**, *861*, 158584.
- [49] M. Siebenhofer, U. Haselmann, A. Nanning, G. Friedbacher, A. E. Bumberger, S. Wurster, W. Artner, H. Hutter, Z. Zhang, J. Fleig, M. Kubicek, *J. Electrochem. Soc.* **2023**, *170*, 014501.
- [50] Y. Bourlier, M. Frégnaux, B. Bérimi, A. Fouchet, Y. Dumont, D. Aureau, *Appl. Surf. Sci.* **2021**, *553*, 149536.
- [51] M. M. Natile, G. Boccaletti, A. Glisenti, *Chem. Mater.* **2005**, *17*, 6272.
- [52] D. R. Mullins, S. H. Overbury, D. R. Huntley, *Surf. Sci.* **1998**, *409*, 307.
- [53] K. Kooser, T. Käambre, M. Vestli, U. Joost, S. Urpelainen, M. Kook, F. Bournel, J. J. Gallet, E. Lust, E. Kukk, G. Nurk, *Int. J. Hydrogen Energy*. **2020**, *45*, 25286.
- [54] H. P. Uppara, J. S. Pasupathy, S. Pradhan, S. K. Singh, N. K. Labhsetwar, H. Dasari, *Mol. Catal.* **2020**, *482*, 110665.
- [55] C. Hanmandlu, A. Singh, M. Karunakara, A. Boopathi, M. Davis, Z. Yu, P. Ding, W. Li, H. Zhao, C. Wu, L. Zhao, B. Dong, S. Wang, *J. Phys. Mater.* **2021**, *4*, 022002.
- [56] S. Biswas, G. Kaur, G. Paul, S. Giddey, *Int. J. Hydrogen Energy*. **2023**, *48*, 12541.
- [57] J. Nielsen, T. Jacobsen, M. Wandel, *Electrochim. Acta.* **2011**, *56*, 7963.
- [58] S. Koohfar, M. Ghasemi, T. Hafen, G. Dimitrakopoulos, D. Kim, J. Pike, S. Elangovan, E. D. Gomez, B. Yildiz, *Nat. Commun.* **2023**, *14*, 7203.
- [59] X. Xu, Y. Pan, Y. Zhong, R. Ran, Z. Shao, *Mater. Horizons*. **2020**, *7*, 2519.
- [60] J. Weese, *Comput. Phys. Commun.* **1992**, *69*, 99.
- [61] S. Dierickx, A. Weber, E. Ivers-Tiffée, *Electrochim. Acta.* **2020**, *355*, 136764.
- [62] A. Nechache, M. Cassir, A. Ringuedé, *J. Power Sources*. **2014**, *258*, 164.
- [63] P. Costamagna, E. M. Sala, W. Zhang, M. Lund Traulsen, P. Holtappels, *Electrochim. Acta.* **2019**, *319*, 657.
- [64] C. Endler-Schuck, J. Joos, C. Niedrig, A. Weber, E. Ivers-Tiffée, *Solid State Ionics* **2015**, *269*, 67.
- [65] C. Endler-Schuck, A. Leonide, A. Weber, S. Uhlenbruck, F. Tietz, E. Ivers-Tiffée, *J. Power Sources*. **2011**, *196*, 7257.
- [66] Y. A. Farzin, A. Weber, M. Harenbrock, D. Nardini, *ECS Trans.* **2023**, *111*, 1987.
- [67] A. Leonide, V. Sonn, A. Weber, E. Ivers-Tiffée, *J. Electrochem. Soc.* **2008**, *155*, B36.
- [68] S. Kanae, Y. Toyofuku, T. Kawabata, Y. Inoue, T. Daio, J. Matsuda, J.-T. Chou, Y. Shiratori, S. Taniguchi, K. Sasaki, *ECS Trans.* **2015**, *68*, 2463.
- [69] S. Golani, F. Wankmüller, W. Herzhof, C. Dellen, N. H. Menzler, A. Weber, *J. Electrochem. Soc.* **2023**, *170*, 104501.
- [70] M. A. Laguna-Bercero, Y. Wang, X. D. Zhou, L. Zhu, *Lect. Notes Energy*. **2023**, *95*, 5.
- [71] T. Zhu, D. E. Fowler, K. R. Poepelmeier, M. Han, S. A. Barnett, *J. Electrochem. Soc.* **2016**, *163*, F952.
- [72] M. Chen, D. Chen, M. Chang, H. Hu, Q. Xu, *J. Electrochem. Soc.* **2017**, *164*, F405.
- [73] H. P. Dasari, S. Y. Park, J. Kim, J. H. Lee, B. K. Kim, H. J. Je, H. W. Lee, K. J. Yoon, *J. Power Sources*. **2013**, *240*, 721.
- [74] Y. A. Farzin, A. Babaei, T. L. Skafte, E. Stamate, A. Ataie, S. H. Jensen, *Solid State Ionics* **2020**, *356*, 115435.
- [75] M. Khoshkalam, Y. A. Farzin, B. H. Sjøln, C. Spezzati, P. Holtappels, I. E. Castelli, B. R. Sudireddy, *Adv. Eng. Mater.* **2024**, *26*, 2302231.
- [76] M. A. Laguna-Bercero, Y. Wang, X. D. Zhou, L. Zhu, *Fundamentals of Solid Oxide Electrolysis Cells (SOEC)*, Springer International Publishing, Berlin **2023**.
- [77] B. Niu, F. Jin, L. Zhang, P. Shen, T. He, *Electrochim. Acta.* **2018**, *263*, 217.
- [78] B. Q. Liu, X. Dong, G. Xiao, F. Zhao, F. Chen, Q. Liu, X. Dong, G. Xiao, F. Zhao, F. Chen, *Adv. Mater.* **2010**, *22*, 5478.
- [79] Y. Huan, Y. Li, B. Yin, D. Ding, T. Wei, *J. Power Sources*. **2017**, *359*, 384.
- [80] B. Wang, Z. Yue, Z. Chen, Y. Zhang, H. Fang, N. Ai, R. Wang, F. Yang, C. Guan, S. P. Jiang, Z. Shao, Y. Luo, K. Chen, *Small* **2023**, *19*, 2304425.
- [81] S. Dey, D. Bose, Y. Akinay, M. Mukhopadhyay, A. Das Sharma, J. Mukhopadhyay, *Surface Modification and Functionalization of Ceramic Composites*, Elsevier, New York **2023**, 255.
- [82] H. Zheng, F. Han, N. Sata, R. Costa, *J. Energy Chem.* **2023**, *86*, 437.
- [83] D. M. Amaya-Dueñas, M. Riegraf, A. Nanning, A. K. Opitz, R. Costa, K. A. Friedrich, *ACS Appl. Energy Mater.* **2022**, *5*, 8143.

- [84] V. Vibhu, I. C. Vinke, F. Zaravelis, S. G. Neophytides, D. K. Niakolas, R. A. Eichel, L. G. J. de Haart, *Energies* **2022**, *15*, 2726.
- [85] A. Sciazko, T. Shimura, Y. Komatsu, N. Shikazono, *J. Therm. Sci. Technol.* **2021**, *16*, JTST0013 .
- [86] Y. Alizad Farzin, O. Mirzaee, A. Ghasemi, *J. Magn. Magn. Mater.* **2014**, *371*, 14.
- [87] K. Cheng, H. Xu, L. Zhang, Y. Du, J. Zhou, S. Tang, M. Chen, *J. Electron. Mater.* **2019**, *48*, 5510.
- [88] S. Molin, J. Karczewski, B. Kamecki, A. Mroziński, S. F. Wang, P. Jasiński, *J. Eur. Ceram. Soc.* **2020**, *40*, 5626.
- [89] F. Tietz, A. Mai, D. Stöver, *Solid State Ionics* **2008**, *179*, 1509.
- [90] D. Klotz, A. Weber, E. Ivers-Tiffée, *Electrochim. Acta.* **2017**, *227*, 110.